

# Radio AGN Activity in Low Redshift Galaxies is Not Directly Related to Star Formation Rates

ARJUN SURESH<sup>1</sup> AND MICHAEL R. BLANTON<sup>1</sup>

<sup>1</sup>*New York University*

## Abstract

We examine the demographics of radio-emitting active galactic nuclei (AGN) in the local universe as a function of host galaxy properties, most notably both stellar mass and star formation rate. Radio AGN activity is theoretically implicated in helping reduce star formation rates of galaxies, and therefore it is natural to investigate the relationship between these two galaxy properties. We use a sample of  $\sim 10^4$  galaxies from the Mapping Nearby Galaxies at APO (MaNGA) survey, part of the Sloan Digital Sky Survey IV (SDSS-IV), along with the Faint Images of the Radio Sky at Twenty centimeters (FIRST) radio survey and the National Radio Astronomy Observatory (NRAO) Very Large Array (VLA) Sky Survey (NVSS). There are 1,126 galaxies in MaNGA with radio detections. Using star formation rate and stellar mass estimates based on Pipe3D, inferred from the high signal-to-noise ratio measurements from MaNGA, we show that star formation rates are strongly correlated with 20 cm radio emission, as expected. We identify as radio AGN those radio emitters that are much stronger than expected from the star formation rate. Using this sample of AGN, the well-measured stellar velocity dispersions from MaNGA, and the black hole  $M$ - $\sigma$  relationship, we examine the Eddington ratio distribution and its dependence on stellar mass and star formation rate. We find that the Eddington ratio distribution depends strongly on stellar mass, with more massive galaxies having larger Eddington ratios. Interpreting our model fit to the data leads to a completeness-corrected estimate of  $F_{\text{AGN}}(\lambda > 0.01)$ , the fraction of galaxies with radio AGN with an Eddington ratio  $\lambda > 0.01$ . At  $\log(M_*/M_\odot) \sim 11$ , we estimate  $F_{\text{AGN}} = 0.03$ . As found in previous studies, the AGN fraction increases rapidly with  $M_*$ , and at  $\log(M_*/M_\odot) \sim 12$  we estimate  $F_{\text{AGN}} \sim 0.36$ . We do not find any dependence on star formation rate, specific star formation rate, or velocity dispersion when controlling for stellar mass. We conclude that galaxy star formation rates appear to be unrelated to the presence or absence of a radio AGN, which may be useful in constraining theoretical models of AGN feedback.

*Keywords:* MaNGA, Eddington Ratio, Maximum Likelihood Estimation

## 1. INTRODUCTION

Active Galactic Nuclei (AGN) are supermassive black holes at the centers of galaxies, shining brightly due to rapid accretion of matter, and detectable across the electromagnetic spectrum. In this paper, we will study radio emitting AGN, which have synchrotron emission that can dominate the mm and cm wavelength spectrum.

Matthews et al. (1964) first noted that radio AGN tend to be in giant elliptical galaxies (specifically in “D” galaxies in Morgan’s classification). Heckman & Best (2014) describe and present the modern evidence confirming this tendency. That review largely builds off of the work of Best et al. (2005a) and Best & Heckman (2012) with the Sloan Digital Sky Survey I and II (SDSS-I, SDSS-II; York et al. 2000), the National Radio Astronomy Observatory (NRAO) Very Large Array

(VLA) Sky Survey (NVSS; Condon et al. 1998), and the Faint Images of the Radio Sky at Twenty centimeters survey (FIRST; Becker et al. 1995).

Those investigations quantified the radio luminosity function as a function of galaxy stellar mass, and showed that the radio luminosity function is a strong function of mass, such that the ratio of radio luminosity to mass grows with mass. Hickox et al. (2009) reported similar effects for radio AGN at  $z \sim 0.25$ – $0.8$  from the AGN and Galaxy Evolution Survey (AGES; Kochanek et al. 2012). This tendency holds for the most luminous radio galaxies (e.g. those with  $\nu L_{\nu, 1.4\text{GHz}}$  above about  $10^{41}$  erg  $\text{s}^{-1}$ ) which are commonly visible also in optical broad lines, but also in the more moderately luminous radio galaxies.

Partly based on these observations, a theoretical picture has emerged that explains the lack of significant

star formation in the most massive galaxies in the universe as a result of the “radio-mode” feedback from the moderately luminous radio jets. Early work implementing radio-mode feedback included Croton et al. (2006), Bower et al. (2006), and Sijacki et al. (2007), but for more comprehensive reviews see Fabian (2012), Somerville & Davé (2015), and Vogelsberger et al. (2020).

In this paper, we revisit the demographics of radio AGN using the integral field survey observations from Mapping Nearby Galaxies at APO (MaNGA; Bundy et al. 2015), a component of the Sloan Digital Sky Survey IV (SDSS-IV; Blanton et al. 2017). MaNGA has a sample of  $\sim 10^4$  galaxies, much smaller than the SDSS-I and -II samples, but with much more reliable and higher signal-to-noise ratio determinations of galaxy properties, including stellar masses, star formation rates, and velocity dispersions, the quantities that will play a key role in our study.

We will use the same techniques as Best et al. (2005c) to match the MaNGA galaxies to NVSS and FIRST and determine radio fluxes. Using the well-measured properties of the MaNGA galaxies will allow us to separate AGN and star formation-driven radio emission accurately. We will quantify the radio activity using the Eddington ratio. Here, the Eddington ratio refers to the ratio of the radio-based estimate of the bolometric luminosity to the black hole mass, the latter estimated using MaNGA’s velocity dispersion.

The Eddington ratio is a somewhat artificial quantity in our context, since the radio luminosity does not directly trace the radiation emitted near the black hole, and the structure of the accretion flow is surely not spherical. However, it is one potentially meaningful way to measure the AGN power relative to the black hole mass.

The measurements we seek are similar to previous results on the distribution of radio AGN luminosities based on SDSS-I, SDSS-II, FIRST, and NVSS (summarized thoroughly by Heckman & Best 2014). Those results showed that the radio luminosity function is a strong function of stellar mass; the characteristic radio luminosity has a greater-than-linear dependence on stellar mass or estimated black hole mass, suggesting that the Eddington ratio distribution also shifts to higher Eddington ratios with mass. Heckman & Best (2014) found that the mean ratio of radio luminosity to stellar or black hole mass varied relatively little with stellar population age (as traced by the  $D_n4000$  measurement of the 4000 Å break; bottom right panel of their Figure 14). However, the measurement shown in that figure is potentially affected by selection effects, because it shows

the ratio of two observed distributions, each affected by different flux selection limits, and neither of which are corrected for those limits. Nevertheless, Janssen et al. (2012) found a similar result, measuring a roughly constant fraction of radio AGN above a fixed luminosity, as a function of star formation rate (using an H $\alpha$  based indicator). In any case, these studies comprise what is a surprisingly small amount of investigation in the literature regarding the important question of how radio AGN luminosity statistically correlates with global galaxy star formation rate.

Using MaNGA integral field spectroscopy from SDSS-IV instead of single-fiber spectroscopy from SDSS-I and SDSS-II yields a smaller sample but a number of advantages relative to the previous efforts just described. We have more precise measurements of central velocity dispersion and stellar mass via the deeper spectra. The star formation rates are more precise and can be measured by adding up the H $\alpha$  emission in only those regions of a galaxy whose emission line ratios are consistent with the presence of star formation (Sánchez et al. 2022). This allows us to avoid confusion between “high excitation radio galaxy emission” (i.e. a simultaneous optical narrow line AGN and radio AGN) and star formation. As we show, the MaNGA Pipe3D star formation rates of Sánchez et al. (2022) also allow us to far more reliably distinguish star formation powered and AGN powered radio emission than the Best & Heckman (2012) sample can using  $D_n4000$ . Finally, our analysis more explicitly accounts for the selection limits in the radio necessitated by the presence of star formation related radio emission.

Section 2 describes the data sets we are using in detail. Section 3 describes our AGN identification method and our methods for fitting and assessing models of the Eddington ratio distribution. In Section 4 we use these methods to fit the parameters of the Eddington ratio distribution and search for a variation of this distribution as a function of galaxy properties. In that section we find that the Eddington ratio distribution depends directly on stellar mass but not directly on any of the other quantities we investigate. We summarize our conclusions in Section 5.

## 2. DATA SAMPLES

### 2.1. Source data: MaNGA, NVSS, and FIRST

In this section we describe the catalogs we use in the study, i.e. MaNGA, the NVSS radio catalog and the FIRST radio catalog. We make use of two different catalogs based on the MaNGA data, the DRPall file (Law et al. 2021) and the Pipe3D Value Added Catalog (Sánchez et al. 2016a, Sánchez et al. 2016b).

The full MaNGA sample of galaxies reduced by the MaNGA Data Reduction Pipeline is summarized in the DRPall file. The catalog contains 11,273 observations of low redshift galaxies ( $z < 0.15$ ). It consists of three main subsamples—Primary, Secondary and Color Enhanced—plus an Ancillary sample. The Primary and Secondary subsamples together comprise  $\sim 83\%$  of the full catalog. These two subsamples are designed to have a uniform distribution in absolute magnitude  $M_i$  (Wake et al. 2017), a rough proxy for the stellar masses of galaxies. The Color Enhanced subsample, on the other hand, is designed to target galaxies that are rare in the NUV- $i$  versus magnitude plane and to provide better statistics for studying them. This sample includes scarce galaxies such as low mass red galaxies or high mass blue galaxies. Wake et al. (2017) provides weights to correct for the sampling rates as a function of galaxy property. We experimented with using these weights in our analysis, but found that doing so has a small but not significant effect on our final results; in part this results because our key analysis regresses against stellar mass and star formation rate. Therefore, for simplicity, we do not use these weights in the analysis we present here.

Out of the 11,273 entries in the DRPall file, only 10,261 correspond to individual galaxies. For these 10,261 entries, we match the MaNGA IFU center to the FIRST and NVSS radio catalogs, to investigate potential radio activity. FIRST is a 1.4 GHz radio source catalog, with integrated flux densities and positions of over a million sources in the sky. It has a flux threshold of 1 mJy, a typical rms of 0.15 mJy, a resolution of 5 arcsec, and subarcsecond positional accuracy, allowing accurate cross-matching with optical catalogs. However, one drawback of the catalog is that its fluxes for extended sources will be underestimated, being resolved out in the relatively high resolution interferometric measurements (Becker et al. 1995). The lower resolution NVSS 1.4 GHz radio catalog is designed to mitigate this issue, with a flux limit of 2.5 mJy and a resolution of 45 arcsec. The combination of NVSS and FIRST allows us to reliably match the MaNGA objects to their radio counterparts and obtain accurate radio fluxes.

Specifically, we follow the procedure outlined in Best et al. (2005c) to identify matches between NVSS, FIRST, and SDSS optical catalogs. Although Best & Heckman (2012) published a set of matches to the SDSS Legacy survey using this procedure complete to 5 mJy, we repeat the analysis here in order to extend the sample to 2.5 mJy and to include additional objects in the MaNGA catalog that did not appear in SDSS Legacy. For a full description of the procedure, we refer the

reader to Section 3 of that paper, but we provide a brief explanation in the next subsection.

## 2.2. Matching MaNGA to NVSS and FIRST

### 2.2.1. General approach

Following Best et al. (2005c), we perform a spatial match of MaNGA galaxies to NVSS, using FIRST to help cross-identify sources and clarify the nature of potential matches.

Around each MaNGA galaxy we collect all NVSS radio sources within a 3 arcmin radius, which is smaller than the typical separation of NVSS sources ( $\sim 9$  arcmin) but large enough to encompass extended or multi-component radio counterparts of the MaNGA galaxy. We refer to galaxies with multiple NVSS matches within this radius as multi-NVSS-component matches and to those with a single NVSS match as single-NVSS-component matches. The multi-component-NVSS sources may be systems such as double jet AGNs without a core component, double jet AGNs with a core component, single jet AGNs with a core component, etc. The single-NVSS-component matches may be any of the above systems but just unresolved by NVSS at their distances. However, due to NVSS’s low positional accuracy, the radio sources may or may not be truly coincident with the MaNGA galaxy and this compels us to invoke FIRST’s high positional accuracy.

FIRST’s high resolution allows a validation of the association of the radio sources with the MaNGA objects. Further matching MaNGA and NVSS with FIRST, up to a radius of 30 arcsec, and by using the rules and criteria provided in Best et al. (2005c), we carefully separate the true matches from the likely fake ones, as explained in somewhat more detail below.

Our procedure differs from that of Best et al. (2005c) in that we use a flux threshold of 2.5 mJy (roughly  $5\sigma$ ), instead of their choice of 5 mJy (roughly  $10\sigma$ ). According to Best et al. (2005c), at  $z \sim 0.1$ , 5 mJy is the value at which the local radio luminosity function begins to be dominated by AGN rather than by star forming galaxies. In this paper however, we choose to maximize the number of radio matches, and use the well measured SFRs from Pipe3D (see below) to distinguish star formation related emission from AGN.

The rules and criteria for different types of sources are briefly provided below. The source types include multi-component-NVSS sources such as “NVSS Doubles”, “NVSS Triples” and single-component-NVSS sources such as “NVSS Singles” with one, two, or more FIRST counterparts. Suitable candidates for each source type are chosen by carefully study-

ing the positions and fluxes of nearby NVSS sources of each galaxy. To keep the discussion brief, we choose not to go into the details of how the candidates are chosen (see Best et al. 2005c for more information). Also, since the rules of source classification are similar for the various source types, we only explain the rules for NVSS Doubles in detail. The rules for the other source types are mentioned briefly. Readers who wish to carry out similar matching procedures should refer to Best et al. (2005c) for a full description.

### 2.2.2. NVSS Doubles

Candidate doubles could potentially be double-jet systems, double-jet plus core systems, or systems where one or both of the NVSS sources are unassociated with the MaNGA galaxy. To accurately identify which of the above possibilities a given candidate belongs to, we do the following:

- To check for a double-jet plus core system, we look for FIRST sources very close to the MaNGA galaxy. If it has a FIRST match within 3 arcsec, we accept the galaxy as a radio source.
- To check for a double-jet system or a double-jet plus core system where the core component is resolved out by FIRST, we look at the proximity of the NVSS sources to the optical galaxy and the angle subtended by the directions from the galaxy toward each source. If both the NVSS sources are within 60 arcsec of the galaxy and the directions subtend an angle  $> 135^\circ$ , we interpret the two sources as two lobes from oppositely-directed jets, and accept the galaxy as a radio source.
- To check if both the sources are physically unrelated, we examine their proximities to the galaxy. If both the sources are at separations  $> 60$  arcsec, it is likely that they are unrelated to the galaxy. Further, we check for FIRST counterparts at separations  $> 15$  arcsec from the galaxy. Such counterparts are not expected to be seen if the two NVSS sources truly are extended features associated with the galaxy, as FIRST would have resolved them out. If instead, three or fewer such counterparts do exist, and their combined flux is more than 50% the combined flux of the NVSS sources, we reject the galaxy as a radio source.
- If only one of the NVSS sources lies within 15 arcsec of the galaxy, we categorize it as a candidate single until further examination (see Sections 2.2.4, 2.2.5, 2.2.6 and 2.2.7).

- Finally, if the galaxy does not satisfy any of the above conditions, it is flagged for visual inspection.

### 2.2.3. NVSS Triples and Quads

Candidate triples could potentially be double-jet plus core systems, double jet systems with an unrelated source, core-jet systems with an unrelated source, etc. The criteria to accurately identify which of the above systems the galaxy belongs to is similar to that of the NVSS Doubles. Candidate triples with a FIRST match within 3 arcsec of the galaxy, we accept as radio sources. We check candidates without a 3 arcsec match for pairs of NVSS sources that could possibly be classified as NVSS Doubles, using the criteria in Section 2.2.2. Further, we reject galaxies as a radio sources using the same method and arguments as that of the doubles. We flag galaxies that were neither accepted nor rejected for visual inspection.

We visually inspected all the candidate quads and candidates with more than four NVSS sources within 3 arcmin in order to classify them. We found that only 2 out of 6 such candidates had at least one of the NVSS truly associated with them.

### 2.2.4. NVSS Single; No FIRST

We accepted as NVSS singles those candidates with the NVSS source within 10 arcsec of the MaNGA galaxy and no FIRST matches within 30 arcsec. These could possibly be either variable AGN that have become much less active between the measurement time frames of NVSS and FIRST, or extended sources whose flux is resolved out by FIRST.

### 2.2.5. NVSS Single; One FIRST

Candidate NVSS Singles with one FIRST source within 30 arcsec could either be just the core of an AGN or an unresolved core-jet system. We accept a candidate galaxy as an NVSS single if it either has a FIRST counterpart within 3 arcsec or a nearby FIRST source that was slightly elongated and pointing towards it. The latter condition allows for the inclusion of core-jet systems unresolved by NVSS.

### 2.2.6. NVSS Single; Two FIRST

Candidate NVSS Singles with two FIRST sources within 30 arcsec could be a core and an unrelated source, a core-jet system or a double-jet system. If one of the FIRST sources lay within 3 arcsec, we accepted the galaxy as a radio source. We also accepted candidates as radio sources if the FIRST counterparts were roughly of the same size, flux and subtended an angle  $> 135^\circ$  at the optical galaxy.

### 2.2.7. NVSS Single; Three FIRST

Candidate NVSS Singles with three FIRST sources within 30 arcsec could be a core and two unrelated sources, double-jet system and an unrelated source, double jet plus core system etc. We carried out the following checks out on each candidate before accepting or rejecting it as a radio source:

- If the galaxy had a FIRST match within 3 arcsec, we accepted it as a radio source.
- We checked each pair of the FIRST sources if they fulfilled the conditions for a FIRST double source (Section 2.2.6). If the galaxy did fulfill the criteria, we accepted it as a radio source.
- If the flux weighted mean position of the three sources lied very close to the galaxy and the farther two sources subtended an angle  $> 135^\circ$  at the closest source, then we accepted the galaxy as a radio source.

At the end of this procedure, we find that 1,126 out of 10,261 MaNGA galaxies are radio sources. For these galaxies, we assign fluxes from the NVSS sources, summing the component fluxes in the cases of multi-NVSS-component sources. We make publicly available this matched catalog, described in Appendix A.

### 2.3. Pipe3D VAC

For the Eddington ratio distribution analysis, we use the Pipe3D catalog of Sánchez et al. (2022). Pipe3D was successfully run on a subset of 10,220 galaxies from DR-Pall, corresponding to a set of unique objects that correspond to galaxies with redshifts in the parent NASA Sloan Atlas (Blanton et al. 2011). The Pipe3D analysis pipeline is based on the FIT3D fitting tool (Sánchez et al. 2016a). This pipeline fits each spaxel’s continuum light with a stellar population modeled as a non-negative linear combination of single stellar populations (SSPs). It uses this model to continuum subtract the spectra to measure the emission lines tracing regions with ionized gas.

For our analysis, we use the integrated stellar mass  $M_\star$  and SFR, estimated in the catalog. We use the SSP-based estimate of  $M_\star$ . For SFR, we work with the  $H\alpha$ -based estimate. This SFR estimate is measured for each galaxy by coadding the  $H\alpha$  contributions from those spaxels whose emission line ratios are consistent with ionization by star formation. Specifically, Sánchez et al. (2022) choose spaxels that lie in the star-forming region of the BPT diagram (Baldwin et al. 1981), using the demarcation specified by Kewley et al. (2001),

and by imposing a minimum  $H\alpha$  equivalent width of 3 Angstrom.

Though the Pipe3D catalog also provides an SSP-based estimate of SFR, we choose to work with the above described  $H\alpha$  estimate of SFR. While the two estimates agree well for galaxies with high  $H\alpha$  based SFR, there is significant discrepancy in the relationship at low  $H\alpha$  based SFR, with the SSP based values usually being relatively overestimated. Nonetheless, we note here that for this study, the SSP based estimate of SFR provides the same result as the  $H\alpha$  based SFR.

### 2.4. MaNGA’s Data Analysis Pipeline

Another key quantity in our study is the central velocity dispersion of stars ( $\sigma_v$ ), which we obtained from MaNGA’s Data Analysis Pipeline (DAP) results. This software package estimates astrophysical quantities from the DRPall datacubes (Law et al. 2021). This DAP includes stellar velocity dispersion determinations using the penalized pixel-fitting method of Cappellari & Emsellem (2004), using nonnegative linear combinations of stellar templates. The DAPall table summarises the results of the DAP, and among other quantities tabulates the DAP stellar velocity dispersion measured within one effective radius ( $R_e$ ) of the galaxy. which is the measure of velocity dispersion we use.

We note that Pipe3D also provides a central velocity dispersion. However, we found that its values were significantly discrepant relative to the DAP values (at the  $\sim 50\%$  level). The relationship between stellar mass and velocity dispersion has more scatter for the Pipe3D values. A consequence of this scatter is that a handful of relatively high stellar mass galaxies (5–10 of them) exist with radio AGN emission, but with low velocity dispersion in Pipe3D. Although these galaxies do not strongly change our overall conclusions, they do induce a small degree of dependence of AGN fraction on velocity dispersion when we use the Pipe3D velocity dispersions, which does not appear using the DAP values (Section 4). We interpret these effects to be a result of errors in the Pipe3D values, and therefore choose to work with the DAP values for  $\sigma_v$ .

### 2.5. Final Sample Definition

To create a sample suitable for our analysis, we start with the 10,220 galaxies in Pipe3D and we exclude the following:

- 2,781 galaxies with  $\sigma_v$  lower than MaNGA’s velocity resolution value of  $65 \text{ km s}^{-1}$ ,
- 582 galaxies with invalid SFRs,
- 477 Ancillary galaxies,

- 85 galaxies that do not have a well-determined redshift,
- 13 galaxies outside the range  $-14 \leq \log_{10}(\text{sSFR}/\text{yr}^{-1}) \leq -9$ ,
- 11 galaxies that are duplicates of galaxies already existing in the catalog,
- 11 galaxies with  $\log_{10}(M_{\star}/M_{\odot}) < 8$  or  $\log_{10}(M_{\star}/M_{\odot}) > 12$ , and
- 5 galaxies with  $\log_{10}(\text{SFR}/M_{\odot} \text{ yr}^{-1}) < -5.5$  or  $\log_{10}(\text{SFR}/M_{\odot} \text{ yr}^{-1}) > 2.5$ .

This process leaves a total of 6,255 galaxies suitable for our analysis of the low redshift radio-AGN Eddington ratio distribution. All of these galaxies were matched to NVSS and FIRST as part of our analysis of the DRPall sample, and 913 have radio matches.

Based on this matching, Figure 1 shows 1.5 arcmin FIRST cutouts of selected radio AGN (see Section 3.2), as a function of host galaxy  $M_{\star}$  and sSFR. The marginal histograms show the number of detected AGN in each bin of  $M_{\star}$  and sSFR. Some of the radio images show well defined jets and lobes that are characteristic of radio AGN (Blandford & Rees 1974, Scheuer 1974). The white panels in the image are bins in which the matched sample does not have any detected AGN. See Section 5 for more detailed comments on the figure.

### 3. METHODOLOGY

This section describes our procedure to distinguish AGN from star formation related emission (Sections 3.1 and 3.2), to estimate Eddington ratios (Section 3.3), and to estimate the Eddington ratio distribution (Section 3.4).

#### 3.1. Star formation related radio emission

In addition to AGN activity, galactic radio emission can stem from free-free and synchrotron processes associated with star formation (Condon 1992). Numerous studies have measured a strong relationship between SFR and radio luminosity (e.g. Condon 1992, Cram 1998, Bell 2003).

Figure 2 shows the MaNGA Pipe3D star formation rates and the NVSS  $L_{1.4 \text{ GHz}} = \nu L_{\nu}$  at  $\nu = 1.4 \text{ GHz}$  for the matching radio detections. The objects on the plot fall into two fairly distinct groups. The well correlated cloud of points at  $\log_{10}(\text{SFR}/M_{\odot} \text{ yr}^{-1}) > 0$  likely have their radio luminosity dominated by star formation. MaNGA’s high precision SFR measurements lead to a reasonably tight relationship between SFR and radio luminosity, with a standard deviation of 0.28 dex,

calculated as described below. For galaxies with emission greatly exceeding that expected from star formation, we ascribe their radio luminosity primarily to AGN activity. The radio-star formation relation therefore allows for a reliable and well-characterized separation of the AGN from star formation related emission.

To compare to previous results, in Figure 2 we show the  $L_{1.4 \text{ GHz}}$ -SFR relation from Hopkins et al. (2003). This relation is linear above  $\log_{10}(L_c/\text{erg s}^{-1}) = 37.95$ , and steeper below that luminosity. Expressed as the inferred SFR as a function of radio luminosity, the relation is

$$\log_{10}(\text{SFR}/M_{\odot} \text{ yr}^{-1}) = \log_{10}(f) - c + \log_{10}(L_{\text{SFR}}/\text{erg s}^{-1}) \quad (1)$$

where:

$$f = \begin{cases} 1 & \text{if } L_{\text{SFR}} > L_c \\ [0.1 + 0.9(L_{\text{SFR}}/L_c)^{0.3}]^{-1} & \text{if } L_{\text{SFR}} \leq L_c \end{cases} \quad (2)$$

We numerically invert this equation to determine the expected luminosity given a MaNGA-based SFR.

To compare to the Pipe3D results we convert the SFR estimate of Hopkins et al. (2003) from their Salpeter (1955) stellar initial mass function (IMF) assumption to Pipe3D’s Chabrier (2003) IMF assumption. Assuming that the SFR determinations are dominated by the massive end of the stellar mass function, we find that the fractional change in SFRs between the two assumptions should be  $\sim -0.25$  dex, which we have applied to the black solid line in Figure 2. This corresponds to the choice  $c = 37.65$  based on the value  $c = 37.4$  found by Hopkins et al. (2003). This shifted relation does not precisely fit the distribution, but since our focus is not on the radio-SFR relation, we will not perform a detailed investigation of this difference here.

Using a fit of a Gaussian distribution to the scatter around the mean relationship, we find a standard deviation of  $\sigma = 0.28$  dex in the luminosity given a SFR.

#### 3.2. Radio AGN identification

A radio detection is defined as a detected AGN if it satisfies one of the following criteria:

- For a galaxy with  $\log_{10}(\text{SFR}/M_{\odot} \text{ yr}^{-1}) < 0$ , we require  $\log_{10}(L_{1.4 \text{ GHz}}/\text{erg s}^{-1}) > 38.6$  to be an identified AGN.
- For a galaxy with  $\log_{10}(\text{SFR}/M_{\odot} \text{ yr}^{-1}) > 0$ , we require  $\log_{10} L_{1.4 \text{ GHz}} > \log_{10} L_{\text{SFR}} + 1$ . Here,  $L_{\text{SFR}}$  is the star formation associated radio luminosity derived from Equation 1. Notice the 1 dex allowance that has been provided.

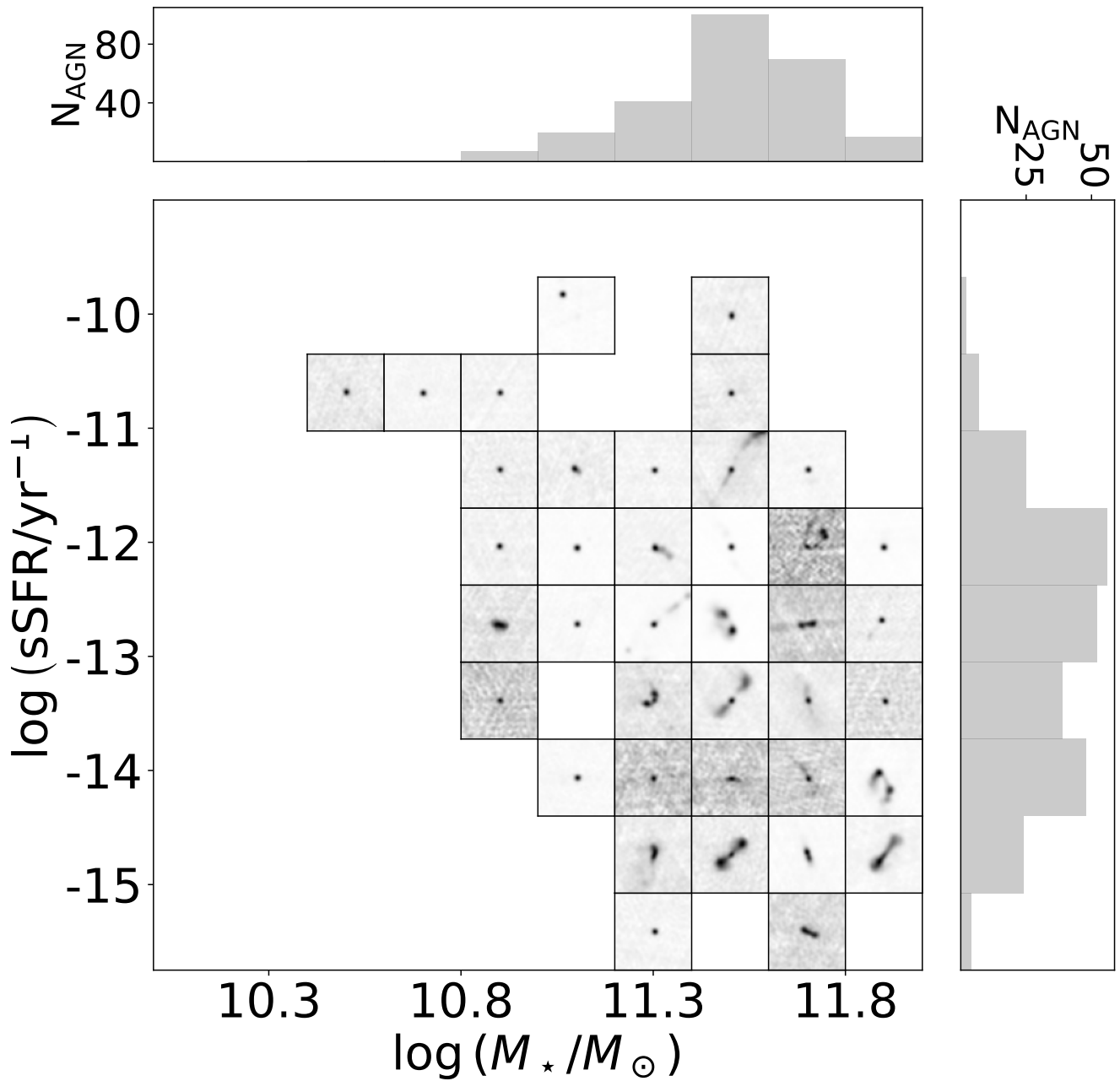


**Figure 1.** FIRST radio cutouts of detected AGN in bins sSFR- $M_*$ , with each cutout spanning 1.5 arcsec on the sky. In each grid of sSFR- $M_*$ , we have chosen a detected AGN to display. The blank locations in the image are locations where our sample does not have detected AGN. At low  $M_*$  ( $\log_{10}(M_*/M_\odot) < 10.4$ ), we see no detected AGN in the sample. At  $10.4 < \log_{10}(M_*/M_\odot) < 11.3$ , the detected AGN mostly seem to be compact sources. And at  $\log_{10}(M_*/M_\odot) > 11.3$ , the AGN population seems to be a mix between compact and extended sources. The purpose of the image is purely for illustration. We do not recommend that any statistical inferences be made based on this image. See Section 5 for more comments on the figure.

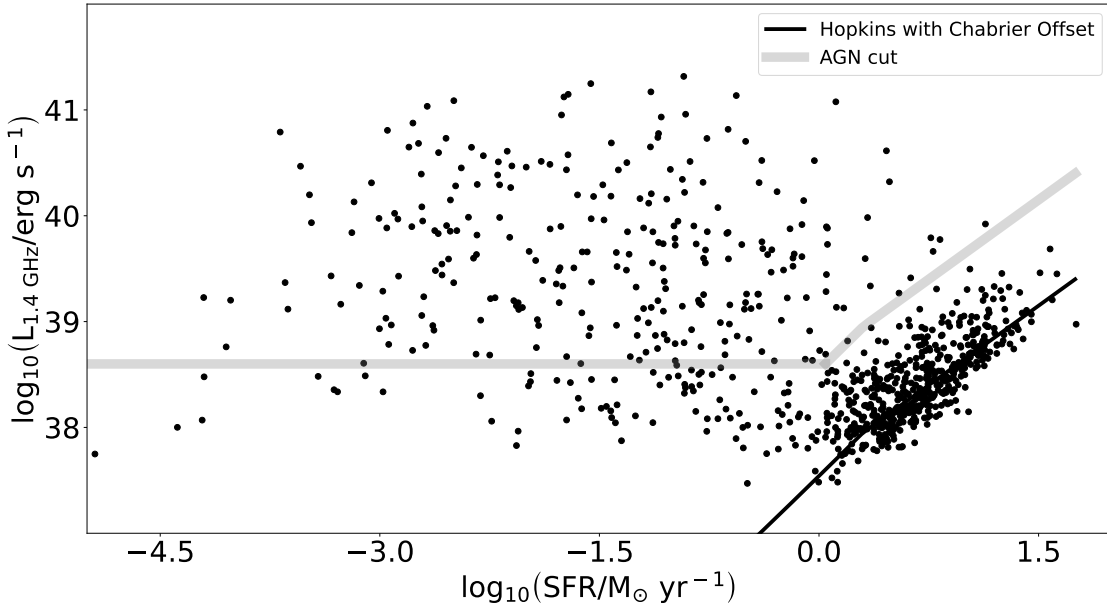


**Figure 2.** Radio luminosity  $\nu L_\nu$  from NVSS at 1.4 GHz and  $H\alpha$  star formation rates from MaNGA. The solid black line shows the relationship found by Hopkins et al. (2003) between radio synchrotron emission and star formation, with an offset to account for the usage of the Chabrier IMF instead of Salpeter. The solid grey line shows the luminosity that must be exceeded for an object to be considered a detected AGN in our analysis.

This criterion is shown in Figure 2 as the solid grey line. The galaxies above this “AGN cut” line are included in the likelihood analysis in Section 4 as detected AGN.

The remainder of the sample consists of galaxies without a detected radio AGN, either because they have no radio detection or because their luminosities fall below our criteria. However, these galaxies may still host AGN that are simply too faint for the 2.5 mJy flux threshold of NVSS, are outshone by the star formation in the galaxy, or just are not luminous enough to exceed the AGN thresholds defined above. For these galaxies, we can determine an upper limit  $L_{\text{lim,AGN}}$  on the radio luminosity that could be associated with an AGN in that galaxy and still not be detected according to our criteria.

To determine these limits, we first use their redshifts and the NVSS flux threshold to determine the radio luminosity upper limit for an NVSS detection,  $L_{\text{lim}}$ . Then the AGN radio luminosity upper limits  $L_{\text{lim,AGN}}$  are defined in the following way:

- For galaxies with  $\log_{10}(\text{SFR}/M_\odot \text{ yr}^{-1}) < 0$ , if  $\log_{10}(L_{\text{lim}}/\text{erg s}^{-1}) < 38.6$ , the AGN upper limit  $\log_{10}(L_{\text{lim,AGN}}/\text{erg s}^{-1})$  is set to 38.6. Otherwise the limit is just  $L_{\text{lim}}$ .
- For galaxies with  $\log_{10}(\text{SFR}/M_\odot \text{ yr}^{-1}) > 0$ , if  $\log_{10}(L_{\text{SFR}}/\text{erg s}^{-1}) + 1 > \log_{10}(L_{\text{lim}}/\text{erg s}^{-1})$ , the AGN upper limit  $\log_{10}(L_{\text{lim,AGN}}/\text{erg s}^{-1})$  is

set to  $\log_{10}(L_{\text{SFR}}/\text{erg s}^{-1}) + 1$ . Otherwise the limit is just  $L_{\text{lim}}$ .

Notice the 1 dex allowance that has been provided in the above definitions.

### 3.3. Eddington ratio measurements

To determine the Eddington ratio of the AGN, we estimate a bolometric luminosity from the radio measurements and a black hole mass from the galaxy velocity dispersion. Both quantities are highly uncertain, but for this investigation our primary purpose for the Eddington ratio is to study the dependence of the radio luminosity in a fashion roughly scaled by black hole mass. The estimated Eddington ratio yields an approximate quantity for this purpose.

We infer the bolometric luminosity from the radio luminosity following the method described by Comerford et al. (2020). We infer X-ray luminosities using the conversion of Panessa et al. 2015:

$$\log_{10}(L_X/\text{erg s}^{-1}) = 0.925 \log_{10}(L_{1.4\text{GHz}}/\text{erg s}^{-1}) + 7.1 \quad (3)$$

We convert this X-ray luminosity to a bolometric luminosity by multiplying by 20, a ratio provided by Comerford et al. (2020).

Measurements of black hole masses based on motions near galactic centers show that black hole mass corre-

lates well with the bulge velocity dispersion of the stars (Gebhardt et al. 2000). To estimate the black hole mass from this relationship we use the previously described  $\sigma_v$  from the DAP and the  $M$ - $\sigma$  determination provided in Gültekin et al. (2009):

$$\log_{10}(M_{\text{BH}}/M_{\odot}) = 8.12 + 4.24 \log_{10}(\sigma/200 \text{ km s}^{-1}) \quad (4)$$

We then calculate the Eddington ratio  $\lambda = L_{\text{bol}}/L_{\text{Edd}}$ , where  $L_{\text{Edd}} = 1.26 \times 10^{38} \times M_{\text{BH}}/M_{\odot} \text{ ergs s}^{-1}$ . For all the objects without a detected AGN we can also determine an upper limit on the Eddington ratio  $\lambda_{\text{lim}}$  based on  $L_{\text{lim,AGN}}$  found above.

### 3.4. Estimating the Eddington Ratio Distribution

We estimate the Eddington ratio distribution  $\phi(\lambda)$  using a maximum likelihood estimator. The data are the set of measured  $\lambda$  values and upper limits  $\lambda_{\text{lim}}$ , and the model we use for the Eddington ratio distribution incorporates possible dependencies on galaxy host properties.

In particular, we choose the Schechter function (Schechter 1976), a power law with an exponential cut off. It is defined as:

$$\phi(\lambda) = \begin{cases} \phi_0 \left(\frac{\lambda}{\lambda_*}\right)^{-\alpha} \exp\left(-\frac{\lambda}{\lambda_*}\right) & \text{if } \lambda \geq \lambda_{\text{min}} \\ 0 & \text{if } \lambda < \lambda_{\text{min}} \end{cases} \quad (5)$$

where  $\phi_0$  is a normalisation constant,  $\alpha$  is a power law index characterizing the faint end slope,  $\lambda_*$  is the Eddington ratio characterizing the drop-off in the distribution at high values, and  $\lambda_{\text{min}}$  is minimum possible value in the distribution.

We allow this Schechter function to depend on galaxy properties through a variation of the faint end slope that depends on the property  $Q$  as:

$$\alpha = \alpha_0 \left(\frac{Q+k}{Q_0}\right)^{\beta}, \quad (6)$$

where we will take:

- $Q = \log_{10}(M_{\star}/M_{\odot})$ ,  $Q_0 = 10.5$  and  $k = 0$  to characterize the mass dependence,
- $Q = \log_{10}(\sigma_v/\text{km s}^{-1})$ ,  $Q_0 = 2.2$  and  $k = 0$  to characterize the velocity dispersion dependence,
- $Q = \log_{10}(\text{SFR}/M_{\odot} \text{ yr}^{-1})$ ,  $Q_0 = 4.5$  and  $k = 5$  to characterize the star formation rate dependence,
- $Q = \log_{10}(\text{sSFR}/\text{yr}^{-1})$ ,  $Q_0 = 2.2$  and  $k = 0$  to characterize the specific star formation rate dependence and,

- $Q = 1$ ,  $Q_0 = 1$  and  $k = 0$  for the case where the model is independent of any galaxy property. We call this the Uniform model.

The values of  $k$  are set so that the numerator remains positive throughout the range of the data.  $Q_0$  is just a pivot point set near the typical value of  $Q + k$  for the data set.

This parametric form can be hard to interpret. The faint-end slope is not directly constrained very well, and  $\lambda_{\text{min}}$  not directly constrained at all, since it remains well below any detectable Eddington ratio. The data constrains a nontrivial combination of the faint-end slope, its dependence on galaxy properties  $\beta$ , and  $\lambda_{\text{min}}$ . The power law dependence of  $\alpha$  on  $Q$  expressed by  $\beta$  allows a large range of different levels of dependence to be modeled, but it is not particularly well motivated nor simple to interpret. We will see in the results below that a more interpretable characterization of the resulting fits is the fraction of galaxies  $F_{\text{AGN}}$  in the model distribution above some specific  $\lambda$  (see Section 4.5).

The likelihood for a single detected AGN becomes:

$$p_i(\lambda_i|\{\alpha_0, \beta, \lambda_*, \lambda_{\text{min}}, Q_i\}) = \phi_{0,i} \left(\frac{\lambda_i}{\lambda_*}\right)^{-\alpha_i} \exp\left(-\frac{\lambda_i}{\lambda_*}\right), \quad (7)$$

where  $\alpha_i$  is defined according to the galaxy property  $Q_i$  and Equation 6, and  $\phi_{0,i}$  is the appropriate normalization value.

The likelihood for a single AGN non-detection is the distribution integrated over the range of possible Eddington ratios:

$$p_i(\lambda_{\text{lim}}|\{\alpha_0, \beta, \lambda_*, \lambda_{\text{min}}, Q_i\}) = \int_{\lambda_{\text{min}}}^{\lambda_{\text{lim}}} d\lambda \phi_{0,i} \left(\frac{\lambda}{\lambda_*}\right)^{-\alpha_i} \exp\left(-\frac{\lambda}{\lambda_*}\right) \quad (8)$$

Over the parameters  $\{\alpha_0, \beta, \lambda_*, \lambda_{\text{min}}\}$ , we maximize the logarithm of the likelihood:

$$\ln \mathcal{L} = \sum_{i=1}^N \ln p_i \quad (9)$$

where  $N = 6,255$  is the total number of galaxies in our sample, and  $p_i$  is calculated using Equation 7 or 8, as appropriate for each galaxy. We minimize  $-\ln \mathcal{L}$ , using the Nelder-Mead algorithm implemented in the `minimize` function in the `optimize` model in SciPy (Virtanen et al. 2020).

We furthermore obtained model error bars by sampling the posterior functions using `emcee`, a Markov Chain Monte Carlo (MCMC) sampler (Foreman-Mackey et al. 2013). Here, the posterior functions were obtained by multiplying the relevant likelihood functions with a

constant prior over a reasonable subspace of the model parameter space. The MCMC was run with 32 independent walkers, a multivariate Gaussian proposal function and a chain length of up to 5000 each.

As a test of our method, we generate fake data drawn from a Schechter distribution and carry out the above described fitting procedure. The procedure was successful in recovering within the estimated error bars the true model parameters that were used to generate the fake data.

## 4. RESULTS: EDDINGTON RATIO DISTRIBUTIONS

### 4.1. Model Parameters

Table 4.1 shows the optimal parameters for each model type  $Q$ , along with their 1 sigma errors.

The  $M_*$  model has a value of  $\beta$  far from zero, suggesting that the Eddington ratio of a radio AGN is heavily dependent on the stellar mass of the host galaxy. Galaxies with high  $M_*$  ( $\log_{10}(M_*/M_\odot) > 10.5$ ) have a significantly greater chance of hosting radio AGNs than the low mass galaxies. This result is in agreement with what Best et al. (2005b) and many other investigators find in their analyses.

The table also shows the difference between the log likelihood values of the  $Q$  models and the Uniform model. Each comparison is equivalent to a likelihood ratio test. In all cases except the sSFR model, the dependence on the auxiliary parameter  $Q$  is highly favored, with the highest significance for  $M_*$ . The sSFR model has a value of  $\beta$  (and  $\ln \mathcal{L}_i - \ln \mathcal{L}_{\text{Unif}}$ ) very close to 0, suggesting that it is not all that different from the Uniform model. Since the models are identical in every respect except for the choice of  $Q$ , these likelihood ratio tests are a meaningful way of comparing the different choices. The table is organised in descending order of model likelihood. Clearly, the  $M_*$  model outperforms the other models by a large margin.

All of the four parameters we study are correlated with each other to some degree in the MaNGA sample. The superiority of the  $M_*$  model relative to the others leads us to ask whether the other three parameters matter at all, or if the detected dependence on SFR and  $\sigma_v$  is just a reflection of how well they are correlated with  $M_*$ . We will examine this question in the following sections, finding that indeed there is little evidence for any dependence on the other parameters at fixed  $M_*$ .

### 4.2. Monte Carlo Samples

To illustrate the results of the model fitting just described, and to answer the question as to whether there is any dependence of the Eddington ratio distribution on

parameters other than  $M_*$ , we will create Monte Carlo samples generated from each of the five model types, and compare them to the observed sample.

To create the MC datasets, we perform the following steps. For each galaxy in each model, we generate  $w = 1000$  Monte Carlo values of radio luminosity, summing a radio AGN component and a SFR-based component:

$$L_{1.4\text{GHz}, \text{MC}} = L_{1.4\text{GHz}, \text{AGN}} + L_{1.4\text{GHz}, \text{SFR}} \quad (10)$$

$L_{1.4\text{GHz}, \text{AGN}}$  is the radio luminosity corresponding to a  $\lambda_{\text{AGN}}$  that is drawn from the Schechter distribution function, for the model under consideration and the value of the appropriate  $Q$  for each galaxy (i.e.  $M_*$ ,  $\sigma_v$ , SFR, sSFR, or none).  $L_{1.4\text{GHz}, \text{SFR}}$  is determined from the SFR using the relationship in Equations 1 and 2, adding Gaussian scatter with a standard deviation of 0.28 dex. The luminosity is converted to flux using the redshift of the galaxy.

Each galaxy in the MC datasets can be classified as one of three possible things, as far as its radio AGN nature is concerned. The first classification is as a detected radio AGN under our criteria for AGN identification (see Section 3.2). The second classification is as a detected radio source but not an AGN detection under our definition. The third classification is as an undetected radio source given NVSS's flux threshold.

For each identified radio AGN in the Monte Carlo, we determine the Eddington ratio  $\lambda_{\text{MC}}$  the same way we do for the observations, using Equations 3 and 4.

Figures 3 and 4 each show one of the 1000 Monte Carlo samples, for the models with  $Q = M_*$  ( $M_*$  model) and  $Q = 1$  (Uniform model) respectively. Figure 3 shows the Monte Carlo  $M_*$  model predicted distributions (bottom panel) and the corresponding observations (top panel). Notice the strong dependence of radio AGN activity on stellar mass in the first column of the figure. This strong dependence reflects the large value of  $\beta$ . Also notice the third column of the first row of the figure. Its distribution is identical to the one in Figure 2. Here however, we choose to show the radio detections in grey and the detected AGN in black. The  $M_*$  model overall looks like it matches the observations well in all of the columns. As in the observations, for the model there are few detected AGN at high SFR or high sSFR. The distribution of the detected AGN in all the columns of the model tends to closely mimic that of the observations. We will characterize this agreement more quantitatively in the following sections.

Figure 4 shows an analogous plot for the Uniform model. While the general trends of the distributions are encapsulated even by this model, it fails to get some of the details right. In particular, it predicts too few

**Table 1.** Schechter function fit parameters to Eddington ratio distributions

Model	$\alpha_0$	$\beta$	$\lambda_*$	$\log_{10} \lambda_{min}$	$\ln \mathcal{L}_i - \ln \mathcal{L}_{Unif}$
$M_*$	$1.95^{+0.11}_{-0.04}$	$-4.99^{+0.27}_{-0.32}$	$0.59^{+0.24}_{-0.07}$	$-4.68^{+0.26}_{-0.17}$	103.76
$\sigma_v$	$1.31^{+0.11}_{-0.02}$	$-1.69^{+0.15}_{-0.20}$	$0.55^{+0.27}_{-0.04}$	$-5.80^{+0.82}_{-0.28}$	56.25
SFR	$1.44^{+0.04}_{-0.04}$	$-0.24^{+0.05}_{-0.05}$	$0.49^{+0.12}_{-0.08}$	$-4.19^{+0.12}_{-0.18}$	12.02
sSFR	$1.42^{+0.03}_{-0.05}$	$0.07^{+0.07}_{-0.11}$	$0.57^{+0.17}_{-0.10}$	$-4.23^{+0.07}_{-0.26}$	0.02
Uniform	$1.42^{+0.03}_{-0.05}$	0	$0.57^{+0.18}_{-0.09}$	$-4.24^{+0.08}_{-0.21}$	0.00

high luminosity AGN ( $\log_{10} (L_{1.4\text{GHz}} / \text{erg s}^{-1}) > 41$ ) relative to the observations. Due to the inability of the model to account for the tight dependence of the activity on  $M_*$ , its distributions contain significantly more scatter than the observations. Furthermore, it fails to distribute the detected AGN in all the columns as similarly to the observations as the  $M_*$  model. Particularly notably, at low  $M_*$  or  $\sigma_v$  there are many more detected AGN in the Uniform model than in the observations.

#### 4.3. Dependence of Eddington Ratio Distribution on Host Galaxy Properties

Figure 5 shows the observed and the  $M_*$ -model- predicted Eddington ratio distributions of detected AGNs as functions of  $M_*$ ,  $\sigma_v$ , SFR and sSFR. The range of each property has been divided into two bins (low and high) and the model is compared to the observed data in both of them. Table 2 lists the low and high bin ranges for the four properties.

For the low and high bins for each property, Figure 5 shows the number of detected AGN  $N_{\text{AGN}}$  in five bins of Eddington ratio, for the observations and also for the expectation value of the  $M_*$  model. We evaluate the expectation value  $\bar{N}_{\text{AGN}}$  as the mean of all of the Monte Carlo samples. We also use the Poisson distribution with a mean  $\bar{N}_{\text{AGN}}$  to determine the expected 68% distribution (i.e. “1- $\sigma$ ”) around the expectation value. This error bar allows us to assess how far away the observations are from the expectations given the best-fit model. Except for one  $\lambda$  bin in the low  $M_*$  bin, the contributions of each bin to the total  $\chi^2$  are of order unity or less. This evidently means that the observations are consistent with being drawn from our best fit model.

In the above mentioned bin, the contribution to  $\chi^2$  value is  $\sim 700$ . This large value is caused due to one detected AGN with  $M_* \sim 10.43$ , whose host galaxy has a very high ellipticity of  $\sim 0.95$ . This can cause the SFR estimate of the galaxy to be imprecise, which if the SFR is highly underestimated would mean that our classification of it as a detected AGN was incorrect. See Section 4.4 for more related comments.

The top left panel shows that the  $M_*$  model successfully predicts that the low mass bins should have no detected AGN (except in the above mentioned bin), which

is something that the other models especially fail to reproduce.

Figures 6, 7, 8, and 9 show analogous plots for the  $\sigma_v$ , SFR, sSFR and Uniform models, respectively (see Table 2 for the property bin ranges). As indicated by the log likelihood ratios in Table 4.1, the  $\sigma_v$  model comes closest to the  $M_*$  model to explaining the observed data. While it manages to do an adequate job in most bins, the model predicts too many detected AGNs in the low SFR and low  $M_*$  bins.

None of the other models explain the observed Eddington ratio distributions satisfactorily. While the models follow the general trends in the number of observed AGN, the values of the observed data do not fall within the estimated uncertainties. Neither the SFR nor the sSFR model perform notably better than the Uniform model, except with respect to the the bins of SFR and sSFR themselves.

The key observation from these distributions is that the  $M_*$  model shown in Figure 5 explains the dependence of the Eddington ratio distribution on every property. It shows no evidence for an additional dependence of the Eddington ratio distribution on any other of the properties. However, the converse is not true; when assessing the other models, each one reveals that there is a required additional dependence on  $M_*$ . The natural interpretation is that the Eddington ratio distribution of the AGN is related primarily to the stellar mass  $M_*$ , and that correlations with other parameters are only due to the secondary effects of their own correlation with  $M_*$ .

#### 4.4. Detected AGN Fraction

In this section, we consider the observed and model-predicted detected AGN fractions in bins of  $M_*$ ,  $\sigma_v$ , SFR and sSFR. Figures 10, 11, 12, 13 and 14 show the detected AGN fractions of the  $M_*$ ,  $\sigma_v$ , SFR, sSFR and Uniform models against each galaxy property.

The AGN fraction in a bin is defined as the number of detected AGN in the bin divided by the total number of galaxies in the bin. The model error bars in each bin correspond to the 1- $\sigma$  limits of the regularised incomplete beta function. This beta function is a generalisation of the CDF of the binomial distribution to a continuous random variable.

**Table 2.** Definition of high and low bins for Figures 5–8.

Property	Low Bin	High Bin
$M_*$	$8.75 < \log_{10}(M_*/M_\odot) \leq 10.44$	$10.44 < \log_{10}(M_*/M_\odot) \leq 12.12$
$\sigma_v$	$1.81 < \log_{10}(\sigma_v/\text{km s}^{-1}) \leq 2.27$	$2.27 < \log_{10}(\sigma_v/\text{km s}^{-1}) \leq 2.72$
SFR	$-5.28 < \log_{10}(\text{SFR}/M_\odot \text{ yr}^{-1}) \leq -1.76$	$-1.76 < \log_{10}(\text{SFR}/M_\odot \text{ yr}^{-1}) \leq 1.76$
sSFR	$-15.85 < \log_{10}(\text{sSFR}/\text{yr}^{-1}) \leq -12.66$	$-12.66 < \log_{10}(\text{sSFR}/\text{yr}^{-1}) \leq -9.53$

These plots do a better job at showcasing the dependence of AGN demographics on host galaxy properties than the previously shown Eddington ratio distribution plots. Whereas we divided the ranges in the Eddington ratio plots (Figures 5–9) into only two bins, we divide them into eight bins here.

Not surprisingly, the  $M_*$  model in Figure 10 outperforms the other models (Figures 11, 12, 13 and 14) in predicting the data. Its predictions are almost perfectly consistent with the observed trends against all the four galaxy properties. The highly negative  $\beta$  value of the model leads to a precise reproduction of the strong observed trends against  $M_*$  (see Figure 10).

Except in a handful of bins (from the left, the third plotted  $M_*$  bin and the first  $\sigma_v$  bin), the contribution towards the  $\chi^2$  is of order unity or lesser. Though those two bins contribute  $\sim 200$  and  $\sim 30$  respectively to the  $\chi^2$ , they contain only  $\sim 1$  detected AGN. Furthermore, the AGN in those bins have host galaxies with very high ellipticities ( $> 0.90$ ). This can affect their measurement of SFR (Sánchez et al. 2022), and hence our radio AGN classification, because our definition of a detected AGN depends on the SFR (see Section 3.2). Imposing an ellipticity cut on the sample resolves many of the above discrepancies, but we choose not to employ that for this study, because we identified this issue *a posteriori*.

Figure 14 shows the fraction plots predicted by the Uniform model. Even this uniform model performs reasonably when evaluated against SFR and sSFR, where it reproduces the general trends of detected AGN fraction. However, it fails to satisfactorily recreate the observed trends against  $M_*$  and  $\sigma_v$ . It is especially bad at predicting the correct AGN fractions at low  $M_*$ , reflecting results similar to those found in Figure 9, and predicting too many detected AGN.

The Uniform model in Figure 14 is interesting to consider in light of what it reveals about how sample selection affects the properties of the detected AGN sample. This model has the same Eddington ratio distribution for all galaxies. However, the black hole mass correlates with  $\sigma_v$ , which itself correlates with the other galaxy properties, and the AGN detections are further affected by selection effects in the sample due to flux limits and our AGN detection limits. These effects lead to a dependence of the detected AGN fraction on galaxy

properties: a strong rise of detection rates with  $\sigma_v$ , a slight rise with  $M_*$ , and a decline with SFR or sSFR. These effects illustrate why explicitly fitting the Eddington ratio distribution accounting for selection effects is so important—as one example, observing a decline of detected AGN fractions as a function of sSFR is not necessarily a sign that high sSFR galaxies have less radio AGN activity (in an Eddington-normalized sense). Accounting for the sample selection is necessary to draw any accurate conclusions.

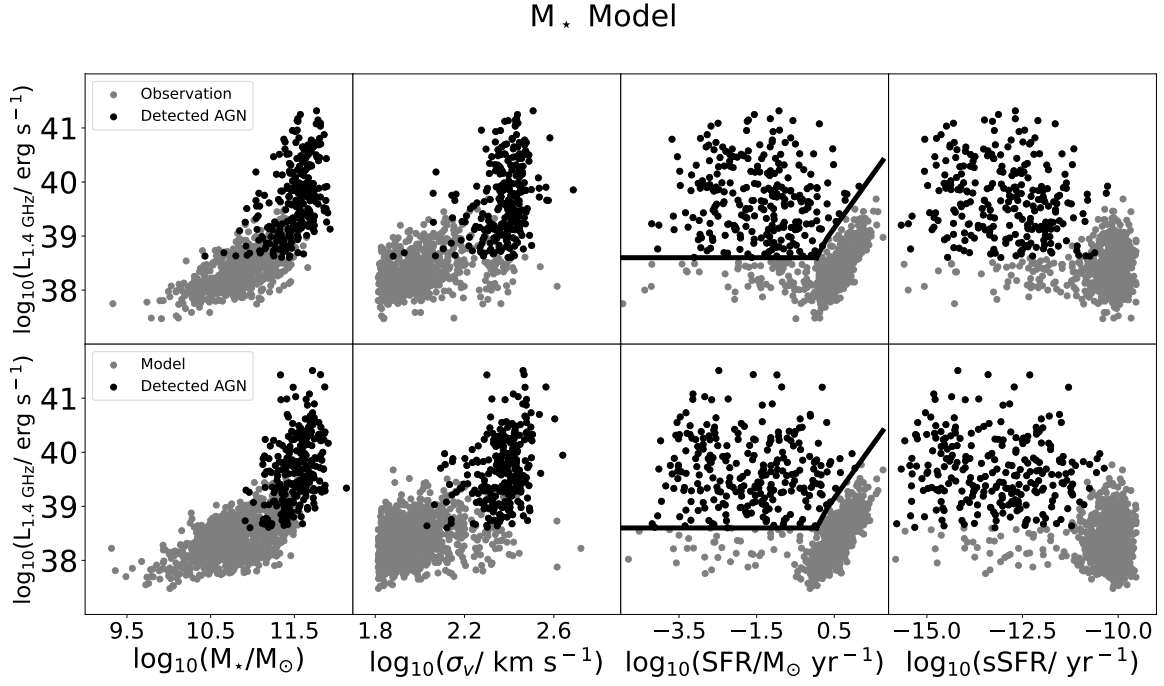
The rest of the models reproduce the observed trends of detected AGN fractions only with respect to the property that the model takes into account. For example, Figure 13 shows that the sSFR-based model explains the sSFR dependence well, but not the other properties. This result reflects similar results to those found for the Eddington ratio distribution in Figure 8.

#### 4.5. Absolute AGN Fraction

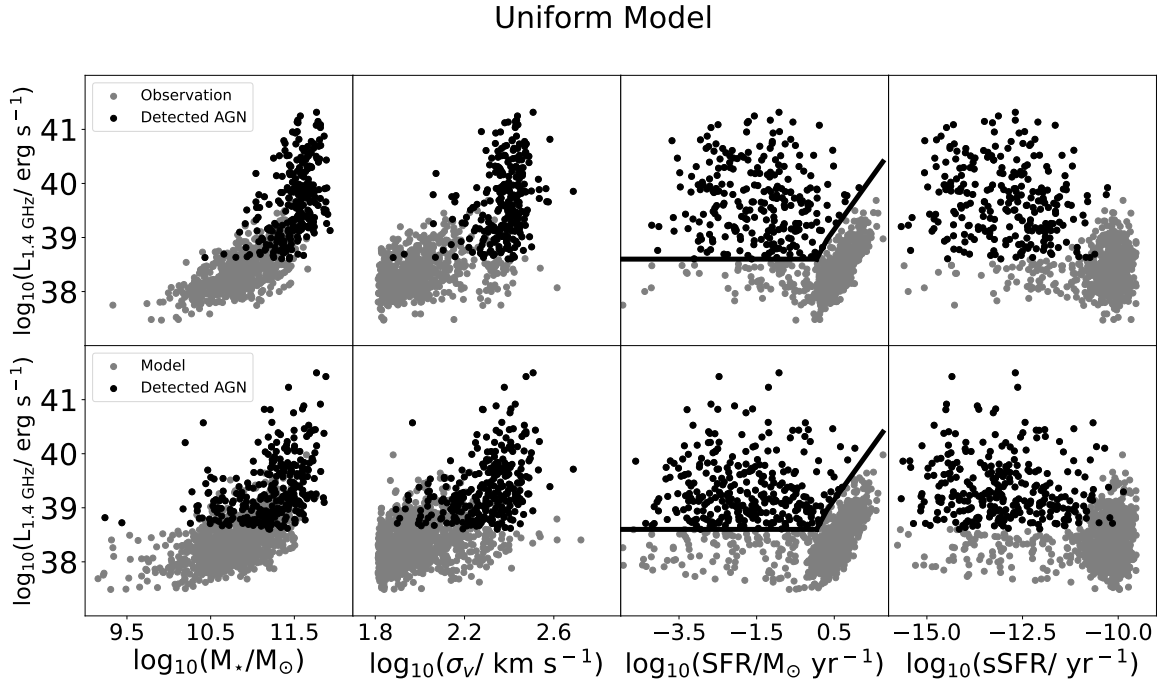
Our model fits allow us to quantify the level of AGN activity as a function of galaxy properties, corrected for the selection effects in the sample, by calculating the fraction  $F_{\text{AGN}}$  of galaxies with  $\lambda > \lambda_c$ , where we will take  $\lambda_c = 0.01$ . The detected fraction  $f_{\text{AGN}}$  is affected by the limits  $\lambda_{\text{lim}}$ , but to the extent that our models are accurate we can simply evaluate them to ask how  $F_{\text{AGN}}$  varies as a function of galaxy properties. It would be misleading to choose  $\lambda_c$  far lower than any  $\lambda_{\text{lim}}$ , and it would sacrifice statistical power to choose  $\lambda_c$  far higher, so the sensible choice is a  $\lambda_c$  similar to the typical  $\lambda_{\text{lim}}$  values. This quantification of the model is more easily interpretable than the model parameters themselves.

Figure 15 shows the  $M_*$  model predicted  $F_{\text{AGN}}$  plotted against  $M_*$ . The error bars correspond to the 68% limits of the possible values of  $F_{\text{AGN}}$  as predicted by different sets of the model parameters [ $\alpha_0$ ,  $\beta$ ,  $\lambda_*$  and  $\log_{10}\lambda_{\text{min}}$ ] that are drawn from the posterior distribution of the MCMC analysis. The general trend of the plot resembles the trend in the top left panel of Figure 10, but here are completeness-corrected to account for the cases where  $\lambda_{\text{lim}} > \lambda_c$ .

We characterize the mass dependence of  $F_{\text{AGN}}$  in the model by fitting a function to Figure 15. This fit is valid in the range  $10 \leq \log(M_*/M_\odot) \leq 12$  and has the following the form:



**Figure 3.**  $L_{1.4\text{GHz}}$  versus  $M_*$ ,  $\sigma_v$ , SFR and sSFR for the observations (top) and the best fit model with  $Q = M_*$  (bottom).



**Figure 4.** Similar to Figure 3, with the bottom row corresponding to the best fit Uniform model.

$$\begin{aligned} \log(F_{\text{AGN}}) &= a_3(\log(M_\star) - 10.5)^3 \\ &+ a_2(\log(M_\star) - 10.5)^2 \\ &+ a_1(\log(M_\star) - 10.5) + a_0 \end{aligned} \quad (11)$$

finding  $a_3 = 0.07_{-0.03}^{+0.03}$ ,  $a_2 = -0.77_{-0.25}^{+0.22}$ ,  $a_1 = 2.44_{-0.57}^{+0.63}$  and  $a_0 = -2.60_{-0.45}^{+0.41}$ .

## 5. CONCLUSIONS

We have examined the relationship between the Eddington ratio distribution of radio AGN activity and galaxy properties for the MaNGA sample matched with the NVSS and FIRST radio surveys. Our results are as follows:

- Explaining the observations requires that the Eddington ratio distribution be a strong function of galaxy stellar mass  $M_\star$ . Figure 15 shows the required dependence in terms of the fraction of AGN with  $\lambda > 0.01$  in the model fit.
- Once the stellar mass dependence is accounted for, there is no evidence for any additional dependence on  $\sigma_v$ , SFR, or sSFR. The agreement of the model with observations in Figures 3, 5, and 10 (and the lack of such agreement for the other models) demonstrates this fact.

The degree of dependence of the detected AGN fraction on other properties is fairly stringently constrained. The variation of the detected AGN fraction across the mass range studied is greater than 2 dex. However, the differences between the observed dependence of the detected AGN fraction on other properties, and that predicted by a model that only depends on stellar mass  $M_\star$ , has an RMS of 0.23 dex (Figure 10). The strong dependence of the Eddington ratio distribution on stellar mass is consistent with many previous studies, as summarized by Heckman & Best (2014). But the taxonomy of AGN in that paper and many others describes the radio-emitting AGN as low sSFR galaxies; to the extent that such a statement is true, it is almost entirely due to the correlation between sSFR and stellar mass, because there is little to no independent correlation of sSFR with radio AGN activity at a given stellar mass.

Surprisingly few studies have directly tested this proposition. As mentioned in the introduction, the lower right panel of Figure 14 in Heckman & Best (2014) shows that the mean ratio of radio luminosity to black hole mass varies little with stellar population age; but in that analysis, the ratio shown has a numerator and denominator affected by different flux limits that are not accounted for, which can affect the results. Janssen et al.

(2012) do examine the radio AGN fraction as a function of SFR at fixed stellar mass and in their Figure 3 find it nearly constant for “low-excitation” radio galaxies (the majority population that are not narrow line AGN); their figure uses radio luminosities  $\nu L_\nu > 10^{40}$  erg s<sup>-1</sup>, so is generally independent of worries about star formation related radio emission (cf. our Figure 2). That paper emphasizes the color dependence of AGN fraction, which is significant at fixed mass; why this dependence exists when the SFR dependence is weak is not entirely clear. The work we describe here improves on these previous studies with superior determinations of star formation rate and a cleaner treatment of selection effects.

Although our finding is that the Eddington ratio distribution is independent of host galaxy SFR, other features of the AGN, such as the radio morphology, might also be. We do not directly quantify the dependence of the radio morphology of AGN on galaxy host properties, but Figure 1 at least does not show any obvious relationship between sSFR and morphology. It does show an obvious dependence of radio AGN activity and morphology with respect to mass. At low  $M_\star$  ( $\log_{10}(M_\star/M_\odot) < 10.4$ ), there are no detected AGN in the sample. At  $10.4 < \log_{10}(M_\star/M_\odot) < 11.3$ , the detected AGN mostly seem to be compact sources. At  $\log_{10}(M_\star/M_\odot) > 11.3$ , the AGN population seems to be a mix of compact and extended sources. The image also shows the lack of such an obvious trend with respect to sSFR. Except in the top two sSFR bins (where there are very little detected AGN), at a given mass, the morphology of the AGN does not change substantially with sSFR. That is, the strong trend of radio AGN morphology with respect to mass seems to exist irrespective of the sSFR of the host galaxy. That being said, we make no claim about the relationship between radio-AGN morphology and host galaxy properties in this study. The quantification of such a relationship requires accurate classifications of all of the radio sources and a more detailed statistical investigation, and we suggest this as an important topic for future study.

Radio AGN are assumed in galaxy formation theories to regulate star formation rates of massive galaxies, and in particular to keep them quenched, as described in the introduction and reviewed by Somerville & Davé (2015). The lack of any relationship between radio AGN activity (in an Eddington ratio sense) and star formation rate may therefore be significant and provides an interesting potential test of these theories. The relevant theoretical predictions, as far as we know, have not been published.

A key aspect of the AGN population is that it manifests in a wide array of fashions across a large dynamic

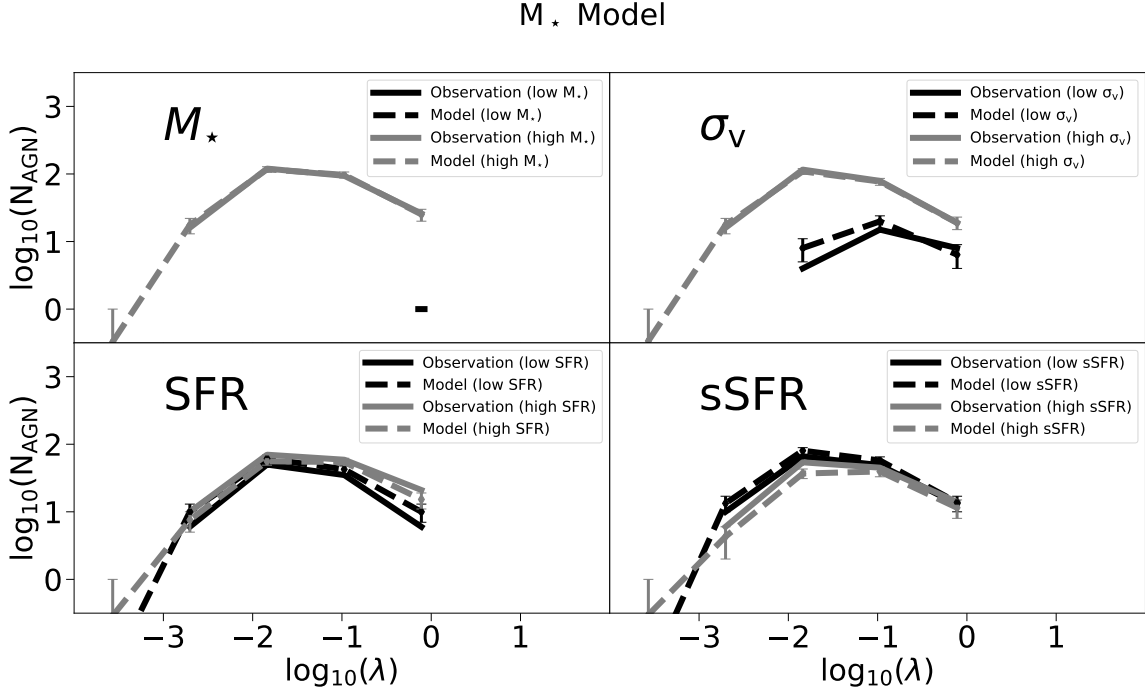


**Figure 5.** Numbers of AGN as a function of Eddington ratio, for two bins (high and low) in each of four properties ( $M_*$ ,  $\sigma_v$ , SFR and sSFR). The solid lines connect the observed number in each bin. The dashed lines show the model expectation value using the  $M_*$  model and the expected  $1-\sigma$  distribution around it.

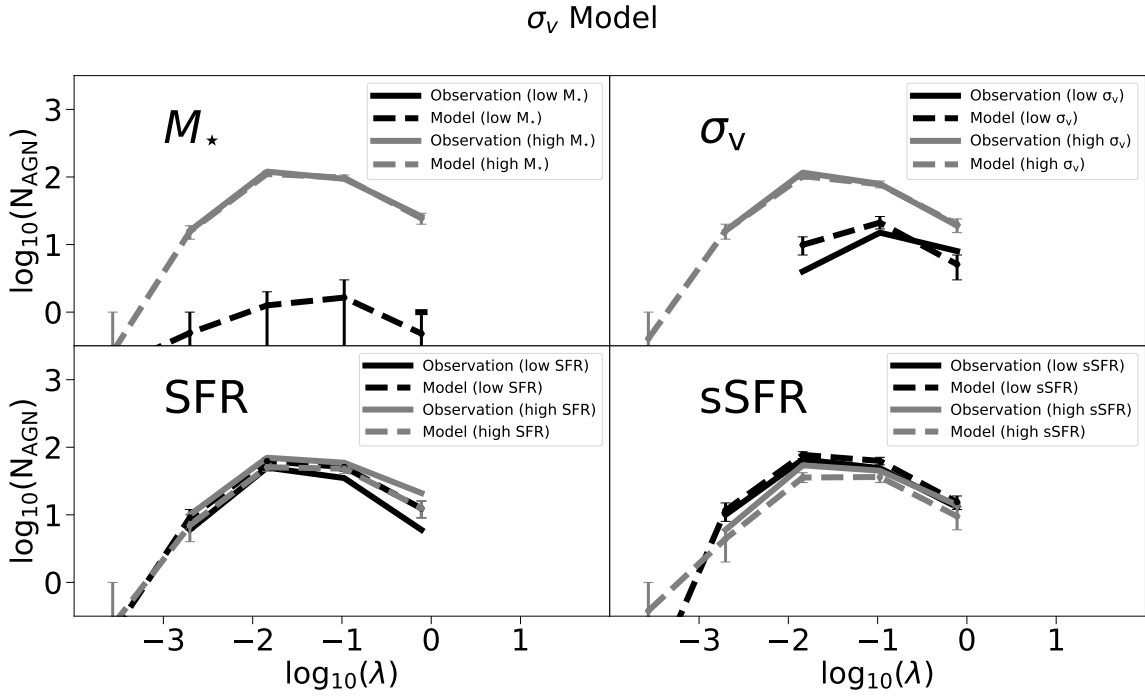


**Figure 6.** Similar to Figure 5, using the  $\sigma_v$  model.

range of wavelengths. They are identifiable in X-rays, UV, optical lines, and the mid-IR, as well as the radio. Yet all of these manifestations are subject to the selection effects analogous to those described here. Despite its relatively small size, with its high quality measurements of galaxy properties, MaNGA sample lends itself to the study of AGN in all their manifestations for very well-understood galaxies, for which characterizing these selection effects is possible. Along with this paper we are publishing the catalog of radio AGN detections and upper limits. We plan to use this catalog in conjunction with detections and limits determined in other signatures in the optical, IR, and X-rays in order to understand the population as a coherent whole.

Funding for the Sloan Digital Sky Survey IV has been provided by the Alfred P. Sloan Foundation, the U.S. Department of Energy Office of Science, and the Participating Institutions.

SDSS-IV acknowledges support and resources from the Center for High Performance Computing at the University of Utah. The SDSS website is [www.sdss4.org](http://www.sdss4.org).

SDSS-IV is managed by the Astrophysical Research Consortium for the Participating Institutions of the SDSS Collaboration including the Brazilian Participation Group, the Carnegie Institution for Science, Carnegie Mellon University, Center for Astrophysics — Harvard & Smithsonian, the Chilean Participation Group, the French Participation Group, Instituto de Astrofísica de Canarias, The Johns Hopkins University, Kavli Institute for the Physics and Mathematics of the Universe (IPMU) / University of Tokyo, the Korean Participation Group, Lawrence Berkeley National Laboratory, Leibniz Institut für Astrophysik Potsdam (AIP), Max-Planck-Institut für Astronomie (MPIA Heidelberg), Max-Planck-Institut für Astrophysik (MPA Garching), Max-Planck-Institut für Extraterrestrische Physik (MPE), National Astronomical Observatories of China, New Mexico State University, New York University, University of Notre Dame, Observatório Nacional / MCTI, The Ohio State University, Pennsylvania State University, Shanghai Astronomical Observatory, United Kingdom Participation Group, Universidad Nacional Autónoma de México, University of Arizona, University of Colorado Boulder, University of Oxford, University of Portsmouth, University of Utah, University of Virginia, University of Washington, University of Wisconsin, Vanderbilt University, and Yale University.

We thank the members of the Hogg-Blanton research group of New York University, Joseph Gelfand and Ingyin Zaw of New York University Abu Dhabi and the BHM-Pop group of SDSS-V, for their valuable insights that have helped shape this study.

## REFERENCES

- Baldwin, J. A., Phillips, M. M., & Terlevich, R. 1981, *PASP*, 93, 5, doi: [10.1086/130766](https://doi.org/10.1086/130766)
- Becker, R. H., White, R. L., & Helfand, D. J. 1995, *ApJ*, 450, 559, doi: [10.1086/176166](https://doi.org/10.1086/176166)
- Bell, E. F. 2003, *ApJ*, 586, 794, doi: [10.1086/367829](https://doi.org/10.1086/367829)
- Best, P. N., & Heckman, T. M. 2012, *Monthly Notices of the Royal Astronomical Society*, 421, 1569–1582, doi: [10.1111/j.1365-2966.2012.20414.x](https://doi.org/10.1111/j.1365-2966.2012.20414.x)
- Best, P. N., Kauffmann, G., Heckman, T. M., et al. 2005a, *MNRAS*, 362, 25, doi: [10.1111/j.1365-2966.2005.09192.x](https://doi.org/10.1111/j.1365-2966.2005.09192.x)
- . 2005b, *MNRAS*, 362, 25, doi: [10.1111/j.1365-2966.2005.09192.x](https://doi.org/10.1111/j.1365-2966.2005.09192.x)
- Best, P. N., Kauffmann, G., Heckman, T. M., & Ivezić, Ž. 2005c, *MNRAS*, 362, 9, doi: [10.1111/j.1365-2966.2005.09283.x](https://doi.org/10.1111/j.1365-2966.2005.09283.x)
- Blandford, R. D., & Rees, M. J. 1974, *MNRAS*, 169, 395, doi: [10.1093/mnras/169.3.395](https://doi.org/10.1093/mnras/169.3.395)

## SFR Model

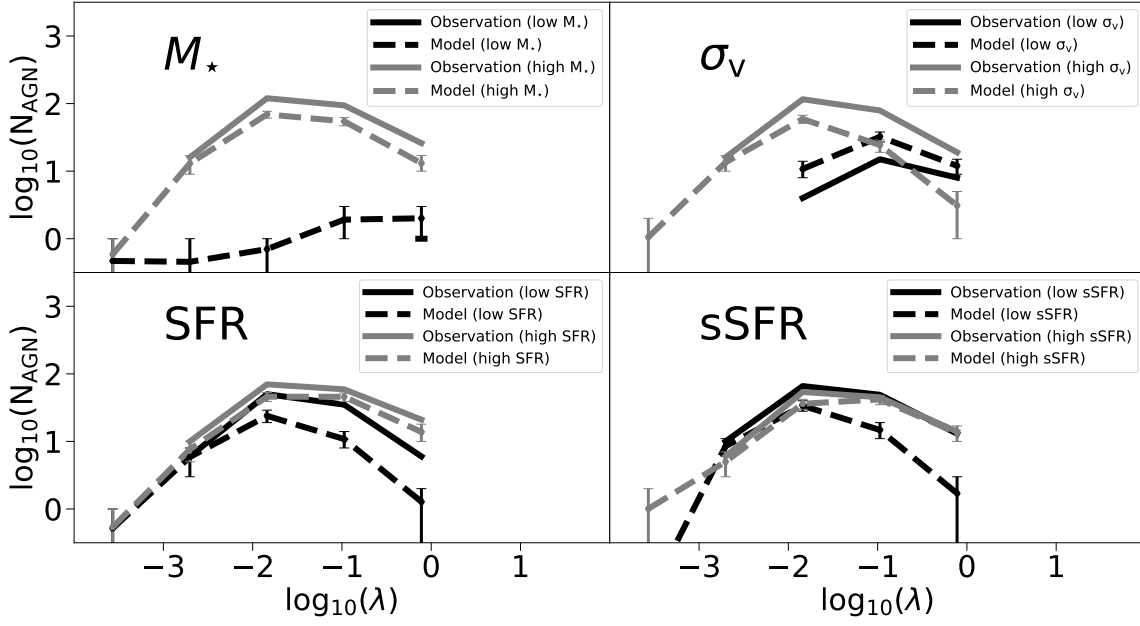


Figure 7. Similar to Figure 5, using the SFR model.

## sSFR Model

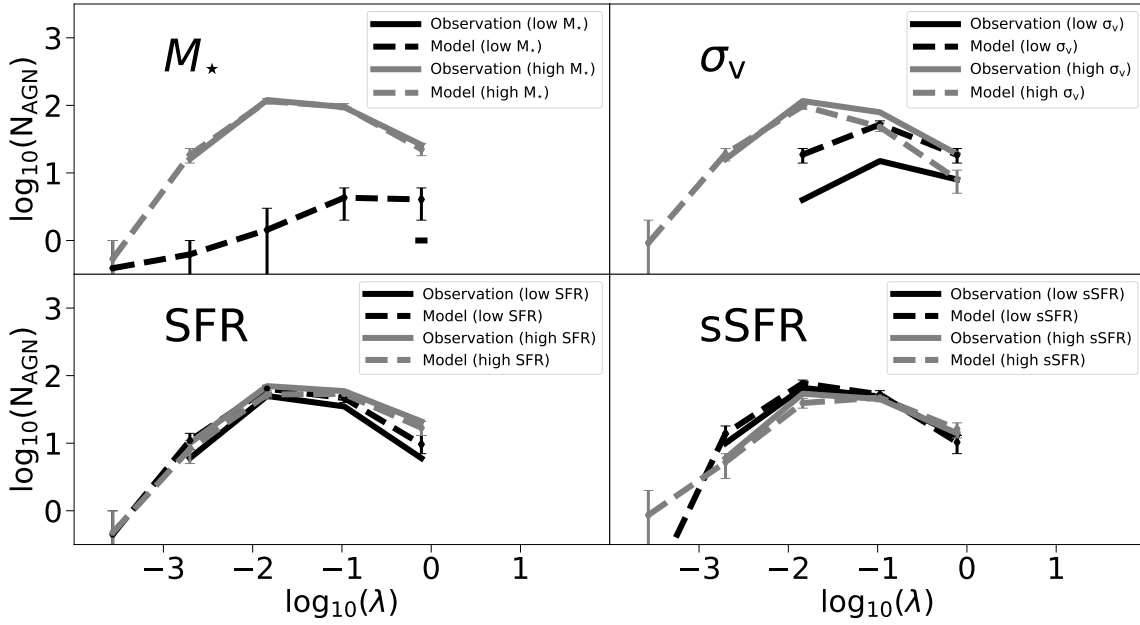


Figure 8. Similar to Figure 5, using the sSFR model.

- Blanton, M. R., Kazin, E., Muna, D., Weaver, B. A., & Price-Whelan, A. 2011, *AJ*, 142, 31, doi: [10.1088/0004-6256/142/1/31](https://doi.org/10.1088/0004-6256/142/1/31)
- Blanton, M. R., Bershady, M. A., Abolfathi, B., et al. 2017, *AJ*, 154, 28, doi: [10.3847/1538-3881/aa7567](https://doi.org/10.3847/1538-3881/aa7567)
- Bower, R. G., Benson, A. J., Malbon, R., et al. 2006, *MNRAS*, 370, 645, doi: [10.1111/j.1365-2966.2006.10519.x](https://doi.org/10.1111/j.1365-2966.2006.10519.x)
- Bundy, K., Bershady, M. A., Law, D. R., et al. 2015, *ApJ*, 798, 7, doi: [10.1088/0004-637X/798/1/7](https://doi.org/10.1088/0004-637X/798/1/7)
- Cappellari, M., & Emsellem, E. 2004, *PASP*, 116, 138, doi: [10.1086/381875](https://doi.org/10.1086/381875)
- Chabrier, G. 2003, *PASP*, 115, 763, doi: [10.1086/376392](https://doi.org/10.1086/376392)
- Comerford, J. M., Negus, J., Müller-Sánchez, F., et al. 2020, *ApJ*, 901, 159, doi: [10.3847/1538-4357/abb2ae](https://doi.org/10.3847/1538-4357/abb2ae)
- Condon, J. J. 1992, *ARA&A*, 30, 575, doi: [10.1146/annurev.aa.30.090192.003043](https://doi.org/10.1146/annurev.aa.30.090192.003043)
- Condon, J. J., Cotton, W. D., Greisen, E. W., et al. 1998, *AJ*, 115, 1693, doi: [10.1086/300337](https://doi.org/10.1086/300337)
- Cram, L. E. 1998, *ApJL*, 506, L85, doi: [10.1086/311651](https://doi.org/10.1086/311651)
- Croton, D. J., Springel, V., White, S. D. M., et al. 2006, *MNRAS*, 365, 11, doi: [10.1111/j.1365-2966.2005.09675.x](https://doi.org/10.1111/j.1365-2966.2005.09675.x)
- Fabian, A. C. 2012, *ARA&A*, 50, 455, doi: [10.1146/annurev-astro-081811-125521](https://doi.org/10.1146/annurev-astro-081811-125521)
- Foreman-Mackey, D., Hogg, D. W., Lang, D., & Goodman, J. 2013, *PASP*, 125, 306, doi: [10.1086/670067](https://doi.org/10.1086/670067)
- Gebhardt, K., Bender, R., Bower, G., et al. 2000, *ApJL*, 539, L13, doi: [10.1086/312840](https://doi.org/10.1086/312840)
- Gültekin, K., Richstone, D. O., Gebhardt, K., et al. 2009, *ApJ*, 698, 198, doi: [10.1088/0004-637X/698/1/198](https://doi.org/10.1088/0004-637X/698/1/198)
- Heckman, T. M., & Best, P. N. 2014, *ARA&A*, 52, 589, doi: [10.1146/annurev-astro-081913-035722](https://doi.org/10.1146/annurev-astro-081913-035722)
- Hickox, R. C., Jones, C., Forman, W. R., et al. 2009, *ApJ*, 696, 891, doi: [10.1088/0004-637X/696/1/891](https://doi.org/10.1088/0004-637X/696/1/891)
- Hopkins, A. M., Miller, C. J., Nichol, R. C., et al. 2003, *ApJ*, 599, 971, doi: [10.1086/379608](https://doi.org/10.1086/379608)
- Janssen, R. M. J., Röttgering, H. J. A., Best, P. N., & Brinchmann, J. 2012, *A&A*, 541, A62, doi: [10.1051/0004-6361/201219052](https://doi.org/10.1051/0004-6361/201219052)
- Kewley, L. J., Dopita, M. A., Sutherland, R. S., Heisler, C. A., & Trevena, J. 2001, *ApJ*, 556, 121, doi: [10.1086/321545](https://doi.org/10.1086/321545)
- Kochanek, C. S., Eisenstein, D. J., Cool, R. J., et al. 2012, *ApJS*, 200, 8, doi: [10.1088/0067-0049/200/1/8](https://doi.org/10.1088/0067-0049/200/1/8)
- Law, D. R., Westfall, K. B., Bershady, M. A., et al. 2021, *AJ*, 161, 52, doi: [10.3847/1538-3881/abcaa2](https://doi.org/10.3847/1538-3881/abcaa2)
- Matthews, T. A., Morgan, W. W., & Schmidt, M. 1964, *ApJ*, 140, 35, doi: [10.1086/147890](https://doi.org/10.1086/147890)
- Panessa, F., Tarchi, A., Castangia, P., et al. 2015, *MNRAS*, 447, 1289, doi: [10.1093/mnras/stu2455](https://doi.org/10.1093/mnras/stu2455)
- Salpeter, E. E. 1955, *ApJ*, 121, 161, doi: [10.1086/145971](https://doi.org/10.1086/145971)
- Sánchez, S. F., Pérez, E., Sánchez-Blázquez, P., et al. 2016a, *RMxAA*, 52, 21. <https://arxiv.org/abs/1509.08552>
- . 2016b, *RMxAA*, 52, 171. <https://arxiv.org/abs/1602.01830>
- Schechter, P. 1976, *ApJ*, 203, 297, doi: [10.1086/154079](https://doi.org/10.1086/154079)
- Scheuer, P. A. G. 1974, *MNRAS*, 166, 513, doi: [10.1093/mnras/166.3.513](https://doi.org/10.1093/mnras/166.3.513)
- Sijacki, D., Springel, V., Di Matteo, T., & Hernquist, L. 2007, *MNRAS*, 380, 877, doi: [10.1111/j.1365-2966.2007.12153.x](https://doi.org/10.1111/j.1365-2966.2007.12153.x)
- Somerville, R. S., & Davé, R. 2015, *ARA&A*, 53, 51, doi: [10.1146/annurev-astro-082812-140951](https://doi.org/10.1146/annurev-astro-082812-140951)
- Sánchez, S. F., Barrera-Ballesteros, J. K., Lacerda, E., et al. 2022, *The Astrophysical Journal Supplement Series*, 262, 36, doi: [10.3847/1538-4365/ac7b8f](https://doi.org/10.3847/1538-4365/ac7b8f)
- Virtanen, P., Gommers, R., Oliphant, T. E., et al. 2020, *Nature Methods*, 17, 261, doi: [10.1038/s41592-019-0686-2](https://doi.org/10.1038/s41592-019-0686-2)
- Vogelsberger, M., Marinacci, F., Torrey, P., & Puchwein, E. 2020, *Nature Reviews Physics*, 2, 42, doi: [10.1038/s42254-019-0127-2](https://doi.org/10.1038/s42254-019-0127-2)
- Wake, D. A., Bundy, K., Diamond-Stanic, A. M., et al. 2017, *AJ*, 154, 86, doi: [10.3847/1538-3881/aa7ecc](https://doi.org/10.3847/1538-3881/aa7ecc)
- York, D. G., Adelman, J., Anderson, John E., J., et al. 2000, *AJ*, 120, 1579, doi: [10.1086/301513](https://doi.org/10.1086/301513)

## Uniform Model

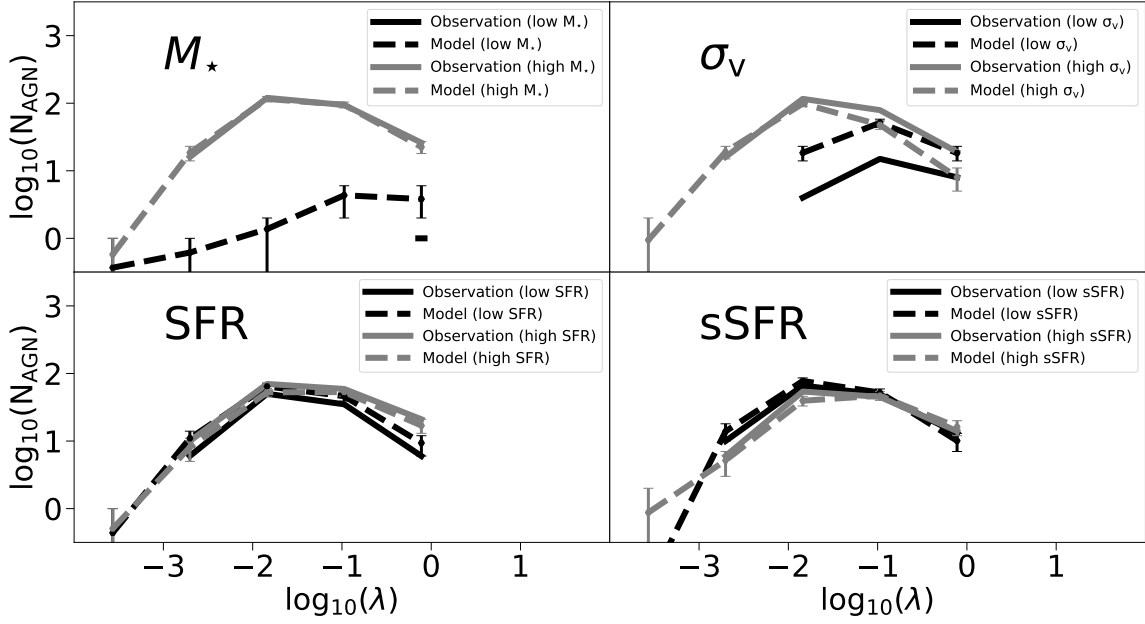
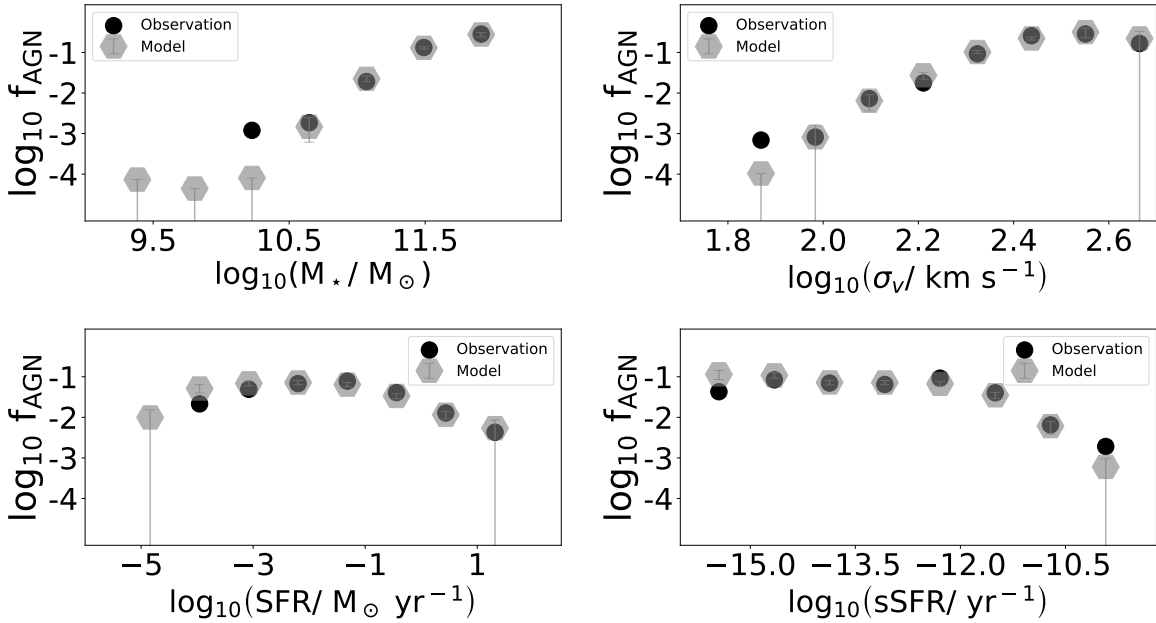
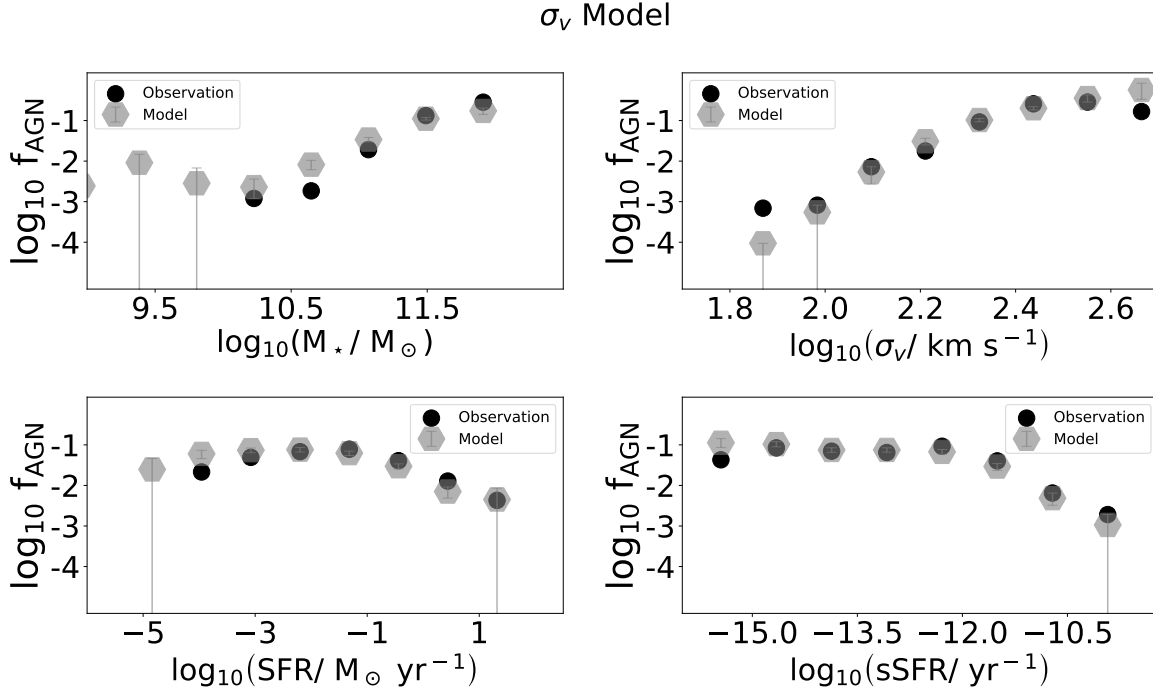


Figure 9. Similar to Figure 5, using the Uniform model.

 $M_*$  Model

**Figure 10.** Detected AGN fraction as a function of  $M_*$ ,  $\sigma_v$ , SFR and sSFR. The grey hexagons show the expectation value based on the best fit model accounting for a dependence on  $M_*$ , with error bars showing the expected 1- $\sigma$  distribution around the expectation value. The black circles show the observations. The model, which only accounts for a dependence on  $M_*$ , explains all of the dependencies of detected fraction as a function of other properties.



**Figure 11.** Similar to Figure 10, with identical observations but an Eddington ratio distribution model that depends only on  $\sigma_v$ . This model explains many qualitative dependencies, but not as quantitatively well as the  $M_*$  model.

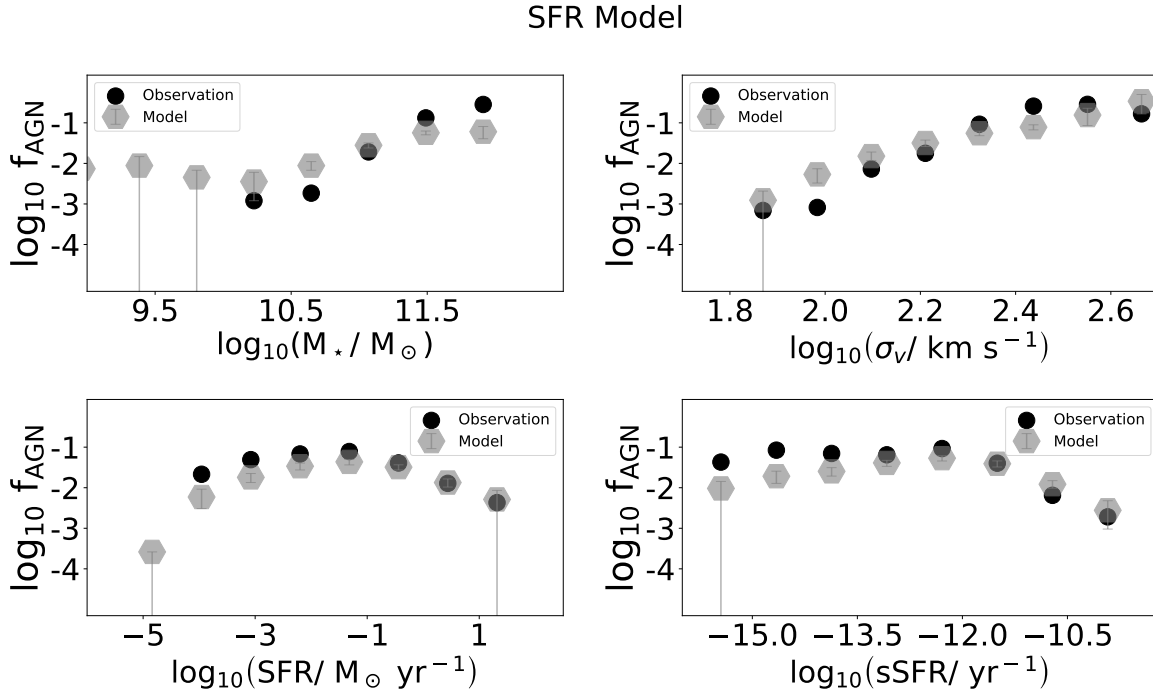


**Figure 12.** Similar to Figure 10, with identical observations but an Eddington ratio distribution model that depends only on SFR. This model does a poor job quantitatively explaining any dependence except for that with SFR.

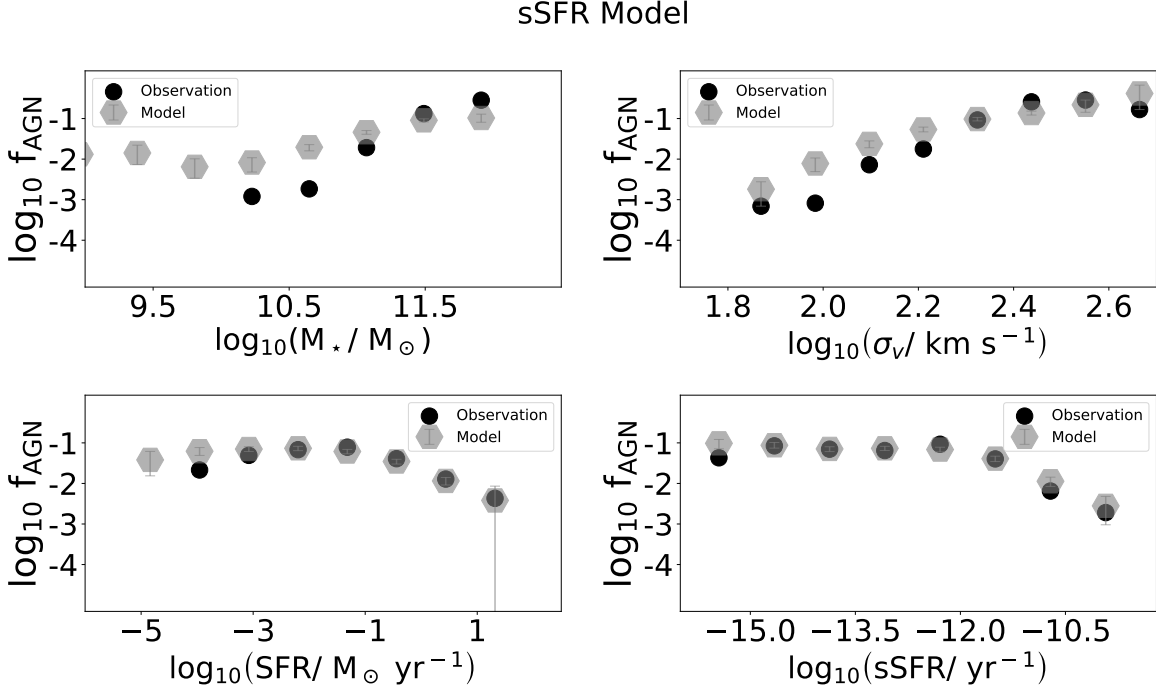


**Figure 13.** Similar to Figure 10, with identical observations but an Eddington ratio distribution model that depends only on sSFR. This model does a poor job quantitatively explaining any dependence except for that with sSFR.

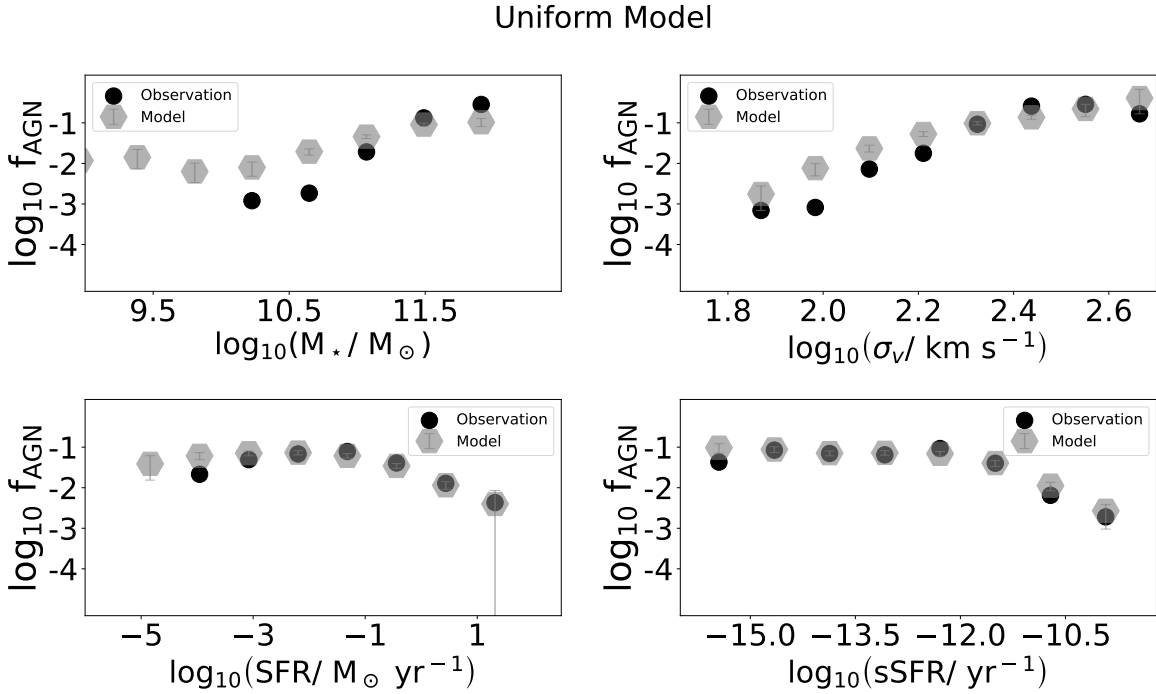


**Figure 14.** Similar to Figure 10, with identical observations but a uniform Eddington ratio distribution model. This model does a poor job quantitatively explaining any dependence, though the qualitative trends are similar to those observed.

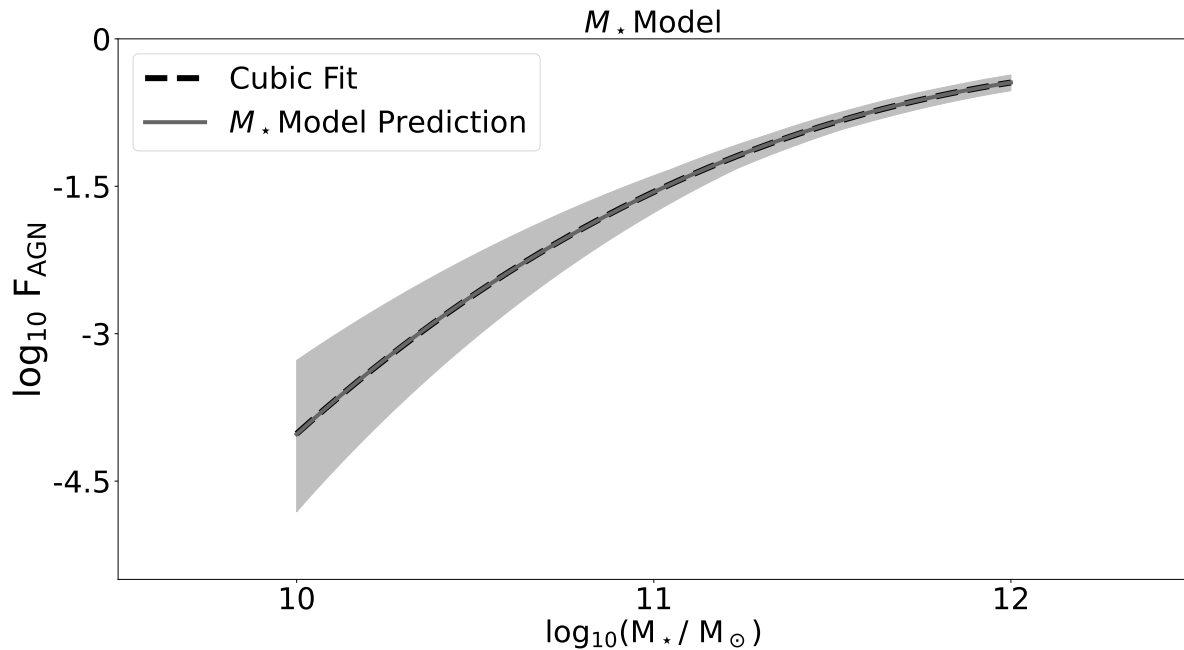


**Figure 15.**  $M_*$  model predictions for the absolute fraction of AGN with  $\lambda > \lambda_c$ , where we will take  $\lambda_c = 0.01$ . To the curve, we fit a cubic polynomial in log-log space, as shown by the dashed line. We quote the coefficients of this fit as a specification of our  $M_*$  model. Note that this relationship between  $F_{\text{AGN}}$  and  $M_*$  is constrained only in the range  $10 \leq \log(M_*/M_\odot) \leq 12$ .

## APPENDIX

## A. APPENDIX

Here we describe the MaNGA-FIRST-NVSS value added catalog (VAC) that is provided along with this paper. This catalog includes 10,261 galaxies in the DRPall file (see Section 2). To this, we match the NVSS and FIRST radio catalogs, down to NVSS’s flux limit of 2.5 mJy. See Section 3 and Best et al. (2005c) for an full explanation of the matching procedure. The columns of the VAC are briefly explained below:

- **mangaid**: Unique ID denoting a particular MaNGA object.
- **plateifu**: Plate and IFU bundle numbers of the measured object, separated by a hyphen.
- **ra**: Right Ascension of the object (J2000). Units - degree.
- **dec**: Declination of the object (J2000). Units - degree.
- **fint**: Total integrated radio flux associated with the galaxy, as measured by NVSS. A dummy value of -999 has been provided for galaxies without radio detections. Units - mJy.
- **fint\_error**: Error in the total integrated radio flux associated with the galaxy, as computed using the NVSS data model (Condon et al. 1998). For multi-component-NVSS matches, the error is the root of the sum of the squares of the errors of individual sources. A dummy value of -999 has been provided for galaxies without radio detections. Units - mJy.
- **log\_lr**: Total radio luminosity of the galaxy after matching with NVSS and FIRST. A dummy value of -999 has been provided for galaxies without radio detections. Units -  $\log(\text{ergs/s})$ .
- **radio\_class**: Following the convention in Best et al. (2005c), we categorise the radio sources as one of five classes. Radio Class 1 is a galaxy that has one NVSS and one FIRST match. Radio Class 2 is a galaxy with one NVSS match but multiple FIRST matches. Radio Class 3 is a galaxy with one NVSS match and no FIRST matches. Radio Class 4 is a galaxy with multiple NVSS matches. Radio Class 0 is a galaxy that isn’t a radio detection.
- **num\_nvss\_3m**: Number of NVSS matches within a 3 arcmin radius of the galaxy.
- **ras\_nvss\_3m**: Right Ascensions of the 3 arcmin NVSS matches. Each object in this column is an array of length six. For the galaxies with less than six 3 arcmin NVSS matches, dummy values of -999 have been provided. The arrays are sorted in descending order of the 3 arcmin NVSS matches fluxes. Units - degree.
- **decs\_nvss\_3m**: Declinations of the 3 arcmin NVSS matches. The column is formatted as above. Units - degree.
- **inds\_nvss\_3m**: Indices of the 3 arcmin NVSS matches as indexed in the NVSS source catalog. The column is formatted as above.
- **fluxes\_nvss\_3m**: Radio flux densities of the 3 arcmin NVSS matches. The column is formatted as above. Units - mJy.
- **flux\_errors\_nvss\_3m**: Radio flux density errors of the 3 arcmin NVSS matches. The column is formatted as above. Units - mJy.
- **num\_first\_30s**: Number of FIRST matches within a 30 arcsec radius of the galaxy.
- **ras\_first\_30s**: Right Ascensions of the 30 arcsec FIRST matches. Each object in this column is an array of length five. For the galaxies with less than five 30 arcsec FIRST matches, dummy values of -999 have been provided. The arrays are sorted in descending order of the 30 arcsec FIRST matches fluxes. Units - degree.

- **decs\_first\_30s**: Declinations of the 30 arcsec FIRST matches. The column is formatted as above. Units - degree.
- **inds\_first\_30s**: Indices of the 30 arcsec FIRST matches as indexed in the FIRST source catalog. The column is formatted as above.
- **fluxes\_first\_30s**: Radio flux densities of the 30 arcsec FIRST matches. The column is formatted as above. Units - mJy.
- **in\_erd\_analysis**: If this value is set to “True”, galaxy was used for the Eddington ratio distribution analysis of this paper. If this value is set to “False”, galaxy was not used for the Eddington ratio distribution analysis of this paper.
- **is\_detected\_agn**: The galaxy hosts a detected radio AGN as defined in Section 3.2, if this column is set to “True”. No detected radio AGN if column is set to “False”.
- **log\_er**: Logarithm of the Eddington ratio of the AGN. See Section 3.3 for more information. A dummy value of -999 has been provided for galaxies that aren’t classified as detected AGN.
- **log\_sfr\_sf**: Integrated Star Formation Rate using only the spaxels compatible with recent star formation, provided by the Pipe3D VAC. A dummy value of -999 has been provided for galaxies that do not have valid values of this quantity in the Pipe3D VAC. Units -  $\log(M_{\odot}/\text{yr})$ .
- **log\_ssfr**: Integrated Specific Star Formation Rate, computed using the Pipe3D VAC. A dummy value of -999 has been provided for galaxies that do not have valid values of star formation rate in the Pipe3D VAC. Units -  $\log(\text{yr}^{-1})$ .
- **log\_mass**: Stellar mass of the galaxy as provided by the Pipe3D VAC. A dummy value of -999 has been provided for galaxies that do not have valid values of this quantity in the Pipe3D VAC. Units -  $\log(M_{\odot})$ .
- **log\_stellar\_sigma\_1re**:  $1 R_e$  Stellar velocity dispersion, as provided by the DAPall file. A dummy value of -999 has been provided for galaxies that do not have valid values of this quantity in the Pipe3D VAC. Units -  $\log(\text{km/s})$ .
- **nsa\_redshift**: Redshift extracted from the NSA catalog.
- **log\_lr\_limit**: Upper limit on the radio luminosity of the galaxies without radio matches. This value based on its redshift and NVSS’s flux threshold of 2.5 mJy. For galaxies with radio detections, the upper limit is just the measured luminosity. A dummy value of -999 has been provided for galaxies where necessary. Units -  $\log(\text{ergs/s})$ .
- **log\_lr\_agn\_thresh**: Threshold radio luminosity that a galaxy would have to reach to be identified as an AGN under our definition (see Section 3.2). A dummy value of -999 has been provided for galaxies where necessary. Units -  $\log(\text{ergs/s})$ .